J. Phys. Chem. A 1999, 103, 9432−9447

Computer Simulation of the Excited State Dynamics of Betaine-30 in Acetonitrile

John Lobaugh and Peter J. Rossky*

Department of Chemistry and Biochemistry, University of Texas at Austin, Austin, Texas 78712-1167

Received: May 17, 1999

Time-dependent studies of the excited state dynamics of betaine-30 in acetonitrile at room temperature have been carried out using a mixed classical/quantum molecular dynamics simulation methodology. The π-electron system of the solute molecule is treated quantum mechanically using the semiempirical Pariser−Parr−Pople Hamiltonian, including the solvent influence on electronic structure. The remaining interactions are treated via empirical potentials. Transition probabilities between adiabatic electronic states are evaluated using surface hopping methods, including all nuclear degrees of freedom in the coupling. The dynamics treats the (rigid) solvent and the dihedral angles for relative rotation of rings of an otherwise rigid solute classically. The contribution of all remaining solute intramolecular vibrations is included in the nonadiabatic coupling via an approximate, but purely quantum mechanical, treatment. Analysis of the dynamics reveals that, after excitation to the first excited state, the energy gap between ground and first excited states of the molecule exhibits an ultrafast (∼100 fs) decrease due to the inertial response of the solvent that accounts for about 70% of the solvent response, followed immediately by a further subpicosecond solvent component. The times and amplitudes of these solvation components are in accord with the results inferred from resonance Raman spectra, and the solvent contribution to the Stokes shift observed is in accord with values inferred from ground state absorption spectral line shape analysis. However, we also find that the energy gap exhibits a slower picosecond time scale response of comparable magnitude due to relative rotation of the central phenolate and pyridinium rings. This relaxation has not been previously noted or incorporated in corresponding electron transfer models. Analysis of contributions to the electronic nonadiabatic coupling shows that this is dominated by a small set of high-frequency intramolecular modes of the betaine-30 molecule, with the solvent making a relatively very small contribution, also in agreement with previous experimental inference.

I. Introduction

Both ultrafast spectroscopy and modern theory have played major roles in the elucidation of the details and mechanisms of intramolecular electron transfer (ET) in solution. In particular, over the last 2 decades, the elucidation of the relative importance of the contributions of solvent dynamics and of intramolecular modes to ET rates is an issue that has been pursued in numerous theoretical and experimental studies.[1] Contemporary theories of ET have typically treated the role of solvent on the level of a dielectric continuum characterized by a Debye relaxation spectrum with a single characteristic relaxation time. The inclusion of inner sphere vibrational modes has been done classically[2,3] or quantum mechanically.[4] A common feature of these theories is that they predict a strong correlation of the ET rate in barrierless cases with the relaxation time characteristic of the solvent.[5−8] Nonetheless, a number of ultrafast ET reactions have been found to exhibit rates that vastly exceed time scales for diffusional solvation dynamics.[9−13] Ultrafast components of solvent dynamics as well as inner sphere modes or intramolecular vibrations have been posited as mechanisms that can give rise to ET times that are faster than solvent diffusional relaxation times.[1,14]

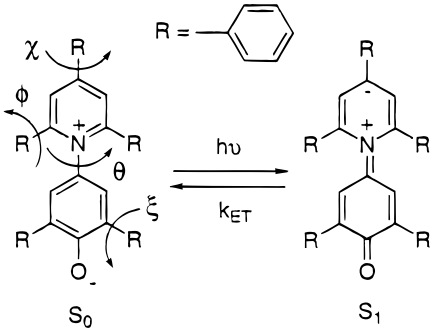

Figure 1. Schematic of the optically induced ground to first excited state electronic transition and the subsequent reverse electron transfer.

A particular molecular solute where the kinetics of ET have been explored in a relatively comprehensive series of experiments is betaine-30. The betaines consist of a covalently bound, charge separated, ground state, shown schematically in Figure 1. The large sensitivity of the lowest energy electronic transition to the local molecular environment has been exploited as the basis for the E_T solvent polarity scales,[15,16] as a probe of micelle/solution interfaces,[17] and as a probe in other applications in analytical chemistry.[18,19] ET occurs after photoexcitation of the highly polar S_0 ground state to the less polar S_1 state of the molecule, as shown schematically in Figure 1. The subsequent kinetics of the photoexcited system have been measured via ultrafast absorption spectroscopy in a series of experiments in polar aprotic solvents[20−26] and alcohols.[11] In these experiments, it was found that the rates for the $S_1 \rightarrow S_0$ relaxation followed characteristic average solvent response times in polar aprotic solvents,[11] with the ET rates in fast aprotic solvents comparable to the solvent dynamical times. However, in slow solvents, these ET rates were found to far exceed inverse solvation times. In alcohols, an additional faster solvent dynamical contribution was inferred to contribute to the ET dynamics.[11]

10.1021/jp991604w CCC: $18.00

The observed ET kinetics of the system have been interpreted in terms of a hierarchy of theoretical formalisms for ET rates which focus on the quantitative role of medium dynamics and of solute intramolecular modes. The limitations and successes of each description in reproducing experimental trends have been effectively used to delineate underlying mechanistic aspects of the rates and to point out remaining uncertainties. It is these uncertainties that motivate large scale simulations of the type we pursue in the present work. To delineate the key open issues, as well as to point out those results that one should expect to be correctly described by a valid model, we briefly review various theoretical modeling efforts. The formulation of Sumi and Marcus[2,3] treats the reaction dynamics via a medium coordinate dependent ET rate with a diffusional evolution of the medium coordinate and treats all modes classically. Application of the formulation, with appropriate modification for the nonequilibrium initial conditions appropriate to the photoinitiated ultrafast experiments,[24] was found to fall short of the observed rates by orders of magnitude. This result was not surprising since the enhancement of the rate of ET in the strongly inverted regime via high-frequency inner sphere/intramolecular modes had been appreciated earlier. In particular, for the inverted regime, high-frequency vibrationally excited states of the product manifold can provide reaction channels with relatively small activation energies. The explicit incorporation of this effect into a theory which also incorporates solvent dynamics (at the level of a single characteristic solvent response time) was accomplished in the formulation of Jortner and Bixon.[4] There, the rate is described as a sum over product vibronic channels of a rate that incorporates solvent diffusional dynamics. Although the rates for the betaine-30 transition evaluated via this formulation were much greater than those obtained via the Sumi–Marcus expression, the rates failed to manifest the apparent transition in the rate-limiting process from solvent dynamical control in fast solvents to one relying primarily on high-frequency intramolecular vibrations at low temperature, where the solvent response is far slower than the ET rate.[24]

A hybrid model formulated by Barbara and collaborators[20,24] incorporates the diffusive dynamics of the Sumi–Marcus model, the vibronic channels of the Jortner–Bixon model, and a very rapidly responding classical intramolecular relaxation of the solute. The low-frequency intramolecular component provides a Gaussian energy width to the individual vibronic channels for any value of the solvent coordinate. This model was able to capture the temperature and solvent dependence of the experimental data in polar aprotic solvents using parameters derived from modeling of static spectra. Nevertheless, it was argued more recently[27,28] that, to properly describe the ET dynamics of these systems, one must include the fact that the solvents relax on multiple time scales, a potential limitation of the simple hybrid model that had been noted by its developers.[24] In particular, it is widely appreciated that the response of polar solvents to rapid perturbation in the solute–solvent interaction includes at least one relaxation time that is far faster than the diffusive time scale of the complete relaxation.[29] This very rapid component can account for a majority of the solvent relaxation dynamics. In many cases, this is the initial so-called inertial, or Gaussian, time scale, but it need not be, as in methanol, where a subpicosecond exponential component is manifest. These results for solvation dynamics have been demonstrated in numerous ways, through experimental transient Stokes shift measurements,[30–33] via molecular dynamics (MD) simulations,[34–36] and via molecular theories of solvation dynamics.[37–40]

If the use of a multiple time scale solvent response is critical, then one could also infer that an important limitation of the Jortner and Bixon vibronic formulation[4] is that to a single average response time, which can be far longer than that actually dominating the dynamics. It has in fact been argued that the regime of solvent response that is critical to the ET rate varies with the size of the activation barrier.[27] In contrast, Bixon and Jortner have presented clear theoretical arguments that activationless ET should, in fact, have only a weak dependence on the excess energy above the diabatic curve crossing.[41] Since the contributing vibronic channels in the strongly inverted regime should correspond to nearly activationless transitions to vibrationally hot ground states, then, by analogy, they argue that rates in the strongly inverted regime also have only a very weak dependence on excess energy, and hence on solvent relaxation dynamics.

In fact, in alcohols,[11] the hybrid model noted above was only able to mimic experiment if the initial conditions for the solvent coordinate were relaxed by a significant fraction essentially instantaneously. These authors attributed this deviation from the original hybrid model to a fast reorganization of the solvent–solute hydrogen bonding, although they tentatively identified the effect on the electronic transition rate with a concomitant change in Franck–Condon factors associated with solute–solvent vibrations, rather than with ultrafast components of the solvation response per se.

Given the discussion above, it is clear that even in this relatively well studied case, important questions remain. The regime where solvent dynamics plays the dominant role is not clearly established, and the importance of alternative time scales for solvent relaxation is unclear. The role of intramolecular vibrations, particularly low-frequency vibrations, is uncertain, and the physical identity of such putative modes is not known. At the most basic level, there is a lack of detail about the potential energy surface on which the ground and excited-state electronic relaxation processes occur prior and after the ET event. Such details would be of great interest in making close and informative connections with recent resonance Raman studies of this system.[42] Such Raman studies can reveal aspects of both solvent dynamics and intramolecular nuclear–electronic couplings. The models discussed above also use only one or two effective vibrational modes. This simplification makes implementation readily accessible, but the validity in describing ET dynamics quantitatively is unknown.

These issues can be addressed by detailed molecular level simulations that include the important quantum mechanical degrees of freedom explicitly and a suitable algorithm to treat nonadiabatic (NA) transitions between states. Here, we develop and implement a practical model and algorithm which includes all intramolecular and solvent degrees of freedom and an explicit treatment of solute electronic structure. The treatment of the electronic problem and its interface with the classical solvent and classical modes of the solute is described in more detail elsewhere;[43] the approach we use is very similar in spirit to that introduced long ago by Warshel and co-workers.[44,45] For the electronic dynamics, we implement the surface hopping method of Tully (molecular dynamics with quantum transitions, MDQT),[46] where the system evolves on one electronic surface at any time and hops stochastically between surfaces based on the state-to-state transition amplitudes. The treatment of high-frequency intramolecular vibrations used here is quite simplified, but the extension to a more realistic treatment is described. The algorithm is applied to the $S_1 \rightarrow S_0$ ET dynamics in acetonitrile. We explore the roles of multiple time scale solvent response and of the underlying solute potential surface and intramolecular modes in the dynamics. We also examine the character of the promoting modes responsible for stimulating the transition, including consideration of *all* solution degrees of freedom.

The paper is organized as follows. In section II, we describe the methodology developed for this study. The methodology represents one of the main contributions of this work. Section III reports and discusses the results derived from the excited-state trajectories of betaine-30. The conclusions are given in section IV. We include a set of appendices that give the details related to the algorithmic development.

II. Methodology

The computational expense of treating even a limited number of degrees of freedom quantum mechanically in a molecular dynamics (MD) simulation necessitates the use of approximate methods of electronic structure. Elsewhere, we have developed a MD model of betaine-30[43] which includes the π electron degrees of freedom of the molecule and treats the remaining electrons and nuclei as effective classical nuclear cores. The π system is treated with the semiempirical Pariser−Parr−Pople (PPP) SCF method[47−49] with single excitation configuration interaction (CI). The intramolecular degrees of freeedom are constrained to be rigid, with the exception of rotation around the six dihedral angles defining the relative orientation of the seven rings (see Figure 1). These angles and the solute center of mass and overall rotation are treated classically. The solvent molecules are also treated classically and modeled by the MD parametrization for acetonitrile of Edwards, Madden, and McDonald.[50] The electrostatic potential produced by the solvent molecules couples to the betaine-30 electronic degrees of freedom via a one electron contribution to the diagonal elements of the Fock matrix. The transition energies are calculated using single CI, which has proven to be very accurate in the PPP method in the calculation of transition energies of heteronuclear aromatic molecules.[51] The model has proven to be accurate in calculating the wavelength, intensity, and bandwidth of the lowest energy transition of betaine-30 in acetonitrile, as well as the shift in these compared to a nonpolar medium.[43] In particular, the width and band shape of the lowest energy absorption (i.e., $S_0 \rightarrow S_1$) are well reproduced by the model when compared to that found from the experimental spectrum in acetonitrile after removal of the vibronic contribution to the band shape found from experiment. These facts indicate that the treatment of the wave function and solvent for the ground and lowest excited states of the molecule in solution are sufficiently accurate for an examination of excited-state relaxation processes.

Calculation of the Excited-State Forces. The reader is referred to ref 43 for complete details of the PPP Hamiltonian used for betaine-30. The derivation of adiabatic excited-state forces, required for the relevant dynamics, using this Hamiltonian is now discussed. The excited-state energies were calculated using single excitation configuration interaction. The single excitation configurational wave functions $|\psi_{i\rightarrow a}\rangle$ have matrix elements

$$\langle\psi_{i\rightarrow a}|(H_{\rm el} - V_\pi)|\psi_{j\rightarrow b}\rangle = \delta_{ij}\delta_{ab}(\epsilon_a - \epsilon_i) + \sum_{\mu\nu} c^j_\mu c^a_\nu (2c^b_\mu c^i_\nu - c^i_\mu c^b_\nu)\gamma_{\mu\nu} \quad (1)$$

where $H_{\rm el}$ is the total *electronic* Hamiltonian, which includes the electron kinetic energy and electron−electron interactions as well as the electron−core and electron−solvent interactions, and the term V_π is the SCF ground-state energy eigenvalue (see eq 2 of ref 43). The terms ϵ_i and $\{c^i\}$ are the molecular orbital (MO) energy and coefficients of the *i*th p-type orbital. The functional form of the two electron repulsion matrix element, $\gamma_{\mu\nu}$, is given by the Mataga−Nishimoto relationship[52] in our calculations. The total energy of the system when the betaine-30 is in the *I*th CI state is given by

$$E^I_{\rm TOT} = K + V_{\rm TOT} + E^I_{\rm CI} \quad (2)$$

where K is the total kinetic energy of the classical degrees of freedom of the system, $V_{\rm TOT}$ is the total ground-state potential, and $E^I_{\rm CI}$ is the *I*th eigenvalue of the CI matrix defined by eq 1. The total ground-state potential is given by

$$V_{\rm TOT} = V_\pi + V_{\rm C-C} + V_{\rm S-S} + V_{\rm C-S} \quad (3)$$

where the terms $V_{\rm C-C}$, $V_{{\rm S}-S}$, and $V_{\rm C-S}$ denote the core−core interactions of the betaine-30, the solvent−solvent, and core−solvent interactions, respectively. Complete details of the terms that make up eq 3 are given in ref 43. When the system is in the *I*th excited state, the force on a nuclear coordinate R (which can be either a solvent or betaine-30 atom) is given by

$$\begin{aligned} F_{\rm R} &= -\frac{\partial}{\partial R}(V_{\rm TOT} + \sum_{mn} C^I_m C^I_n A_{nm}) \\ &= -V^{(R)}_{\rm TOT} - \sum_{mn} C^I_m C^I_n \frac{\partial}{\partial R} A_{nm} \end{aligned} \quad (4)$$

where the CI energy has been rewritten in terms of its eigenvector coefficients $\{C^I\}$ and matrix elements given by eq 1, where an excitation involving promotion of an electron from an occupied orbital i to an unoccupied orbital a has been replaced by a single index n. Accordingly, the *I*th CI eigenvector vector is written as

$$|\Psi_I\rangle = \sum_n C^I_n |\psi_n\rangle \quad (5)$$

The symbol $X^{(R)}$ (e.g., $V^{(R)}$ in eq 4) denotes that the derivative is taken with respect to R while neglecting the coordinate dependence of the MO coefficients in X in evaluating the derivative. As noted elsewhere,[53,54] the ground-state SCF energy is a varitional minimum with respect to the MO coefficients; hence, no terms due to gradients of the molecular orbital expansion coefficients contribute to the ground-state nuclear forces (i.e., $\partial/\partial R\ V_{\rm TOT} = V^{(R)}_{\rm TOT}$). Likewise, the CI energy is a variational minimum with respect to the CI eigenvector coefficients; hence, their coordinate dependence can be neglected in eq 4. However, derivatives of the matrix elements A_{nm} require evaluation of gradients of the MO coefficients. These can be approached through the use of the coupled perturbed Hartree−Fock (CPHF) equations,[55] wherein a derivative of a MO coefficient is rexpressed in terms of derivatives of unitary transformation matrix elements:

$$\frac{\partial c^a_\mu}{\partial R} = \sum_l c^l_\mu u^R_{la} \quad (6)$$

The sum in the above equation extends over both real and virtual MOs. Using this relation, the final term of eq 4 can be shown to be[53,56]

$$\sum_{mn} C^I_m C^I_n \frac{\partial}{\partial R} A_{nm} = \sum_{mn} C^I_m C^I_n A^{(R)}_{nm} + 2\sum_{ks} u^R_{ks} \zeta^I_{ks} \tag{7}$$

where the sum over m,n is over the space of one-electron excitaions, the sum over k,s is over all occupied and unoccupied molecular orbitals, and ζ^I is the Lagrangian matrix where the changes of CI energy with respect to the MO coefficients are collected. Note that the matrix ζ^I is independent of which particular nuclear derivative is being calculated and need only be calculated once. It is, however, a function of the CI eigenvector coefficients $\{C^I\}$ and therefore must be calculated for each CI state. The first-order unitary transformation matrix derivatives are found through solving the CPHF equations, which for a closed-shell system are written as[55]

$$(\epsilon_p - \epsilon_q) u^R_{qp} = B^R_{qp} + \sum_a^{\text{virtual}} \sum_i^{\text{real}} A_{ai,qp} u^R_{qp} \tag{8}$$

where the vector $\mathbf{B}^R$ and matrix $\mathbf{A}$ are given in Appendix A. The efficient computation of the term $2\sum_{ks} u^R_{ks}\zeta^I_{ks}$ using the so-called Z vector method is also outlined in Appendix A.

Elements of the Nonadiabatic Dynamics Method. In this section, the details and algorithm for implementing the MDQT method[46] in the present context are described. We first outline how the method is implemented with the MD model for betaine-30 and the PPP semiempirical electronic structure approach used for the electronic degrees of freedom. In the MDQT method, or in adiabatic dynamics, the single state adiabatic force given by eq 4 is used to evolve the nuclear trajectory. The Schrödinger equation for the electronic degrees of freedom $\mathbf{r}$ for a given configuration of nuclear coordinates $\mathbf{R}$ is given by

$$H_{\text{el}}(\mathbf{R};\mathbf{r})|\Psi_I(\mathbf{R};\mathbf{r})\rangle = (E^I_{\text{CI}}(\mathbf{R}) + V_\pi(\mathbf{R}))|\Psi_I(\mathbf{R};\mathbf{r})\rangle \tag{9}$$

Here, the quantum mechanical state of the system is expanded in the adiabatic CI states

$$|\Phi(\mathbf{R},\mathbf{r},\mathbf{t})\rangle = \sum_I B_I(t)|\Psi_I\rangle \tag{10}$$

Using the time-dependent Schrödinger equation, equations of motion for the expansion coefficients, $B_I(t)$, can be derived

$$i\hbar\dot{B}_I = B_I(E^I_{\text{CI}} + V_\pi) - i\hbar\sum_J B_J \dot{\mathbf{R}}\cdot\mathbf{d}_{IJ} \tag{11}$$

where $\mathbf{d}_{IJ}$ is the NA coupling vector given by

$$\mathbf{d}_{IJ} = \langle\Psi_I|\nabla_R\Psi_J\rangle \tag{12}$$

It should be noted that the ground state is included in the total expansion of the wave function in the above expansion. Since the ground-state Slater determinant does not couple to the single excitation configurations, we have, using the notation in eq 5,

$$|\Psi_0\rangle = \sum_n C^0_n|\psi_n\rangle = C^0_0|\psi_0\rangle = |\psi_0\rangle \tag{13}$$

where $|\psi_0\rangle$ is the ground-state Slater determinant.

For numerical convenience, one can define

$$\tilde{B}_I = B_I \exp\left(\frac{i}{\hbar}\int_0^t \mathrm{d}t' V_\pi\right) \tag{14}$$

Equation 11 then becomes

$$i\hbar\dot{\tilde{B}}_I = \tilde{B}_I E^I_{\text{CI}} - i\hbar\sum_J \tilde{B}_J \dot{\mathbf{R}}\cdot\mathbf{d}_{IJ} \tag{15}$$

The NA coupling vector can be expressed in a form suitable for the semiempirical formulation used here by expanding the CI states in terms of their electronic configurations as given in eq 5

$$\begin{aligned}\mathbf{d}_{IJ} &= \sum_{nm} C^I_n \nabla_R C^J_m \langle\psi_n|\psi_m\rangle + \sum_{nm} C^I_n C^J_m \langle\psi_n|\nabla_R\psi_m\rangle \\ &= \sum_n C^I_n \nabla_R C^J_n + \sum_{nm} C^I_n C^J_m \langle\psi_{\text{n}}|\nabla_R\psi_m\rangle\end{aligned} \tag{16}$$

The first term of eq 16 can be further simplified by using the fact that the CI states diagonalize the Hamiltonian within the space of one-electron excitations, viz.,

$$\langle\Psi_I|(H_{\text{el}} - V_\pi)|\Psi_J\rangle = 0 \tag{17}$$

Taking the derivative of this expression, we have

$$\begin{aligned}&\nabla_R\langle\Psi_I|(H_{\text{el}} - V_\pi)|\Psi_J\rangle \\ &\quad= \sum_{mn} \nabla_R C^I_n C^J_m A_{nm} + \sum_{mn} C^I_n \nabla_R C^J_m A_{nm} + \sum_{mn} C^I_n C^J_m \nabla_R A_{nm} \\ &\quad= E^J_{\text{CI}} \sum_n C^J_n \nabla_R C^I_n + E^I_{\text{CI}} \sum_m C^I_m \nabla_R C^J_m + \sum_{mn} C^I_n C^J_m \nabla_R A_{nm}\end{aligned} \tag{18}$$

Then, using the orthonormality of the CI states, one can show that

$$\sum_n C^J_n \nabla_R C^I_n = -\sum_n C^I_n \nabla_R C^J_n \tag{19}$$

Substituting this relation into eq 18 and rearranging terms, it can be shown that the first term of eq 16 can be written as

$$\sum_n C^I_n \nabla_R C^J_n = \frac{\sum_{mn} C^I_n C^J_m \nabla_R A_{nm}}{(E^J_{\text{CI}} - E^I_{\text{CI}})} \tag{20}$$

Simplification of the gradient terms $\langle\psi_n|\nabla_R\psi_m\rangle$ in the second term in eq 20 is done in Appendix B. The gradient terms $\langle\psi_n|\nabla_R\psi_m\rangle$ are zero if the wave functions differ by more than one spin−orbital. Hence, the only nonzero terms in the second term in eq 16 will be (see Appendix B)

$$\begin{aligned}\langle\psi_{i\to a}|\nabla_R\psi_0\rangle &= \sqrt{2}\sum_\mu c^i_\mu \nabla_R c^a_\mu \\ \langle\psi_{i\to \text{b}}|\nabla_R\psi_{i\to a}\rangle &= \sqrt{2}\sum_\mu c^b_\mu \nabla_R c^a_\mu \\ \langle\psi_{i\to a}|\nabla_R\psi_{j\to a}\rangle &= \sqrt{2}\sum_\mu c^j_\mu \nabla_R c^i_\mu\end{aligned} \tag{21}$$

As with the calculation of the adiabatic force, the derivatives in the above equation can be expanded in terms of the unitary transformation matrix elements. Combining these results the components of the NA coupling vector can be written

$$\begin{aligned}\left\langle \Psi_I \middle| \frac{\partial}{\partial R}\Psi_J \right\rangle &= d^R_{IJ} \\ &= \sum_n C_n{}^I \frac{\partial}{\partial R} C^J_m + \sum_{nm} C^I_n C^J_m \left\langle \psi_n \middle| \frac{\partial}{\partial R}\psi_m \right\rangle \\ &= \frac{\sum_{mn} C^I_n C^J_m \frac{\partial}{\partial R} A_{nm}}{(E^J_{\mathrm{CI}} - E^I_{\mathrm{CI}})} + \sum_{nm} C^I_n C^J_m \left\langle \psi_n \middle| \frac{\partial}{\partial R}\psi_m \right\rangle \\ &= \frac{\sum_{mn} C^I_n C^J_m A^{(R)}_{nm}}{(E^J_{\mathrm{CI}} - E^I_{\mathrm{CI}})} + 2\sum_{ks} u^R_{ks}\zeta^{IJ}_{ks}\end{aligned} \tag{22}$$

where the changes of the MO coefficients with respect to the nuclear coordinate in the NA coupling from the first and second terms of eq 16 have been collected in the vector ζ^{IJ}. The vector ζ^{IJ} is a function of the CI eigenfunction coefficients $\{C^I\}$ and $\{C^J\}$. The efficient calculation of the term $2\sum_{ks} u^R_{ks}\zeta^{IJ}_{ks}$ can be carried out using a modification of the Z vector method of Handy and Schaefer[56] and is outlined in Appendix A.

The high-frequency intramolecular degrees of freedom of betaine-30 play an important role in determining the absorption width of the S_0 to S_1 transition by giving rise to a vibronic progression which is manifest as a broadening of the absorption on the high-frequency side. An estimate of the corresponding inner sphere reorganization energy found from fits of the absorption spectrum is approximately 720 cm^{-1} with a single effective frequency of approximately 1600 cm^{-1}.[20] This effective quantum mechanical mode also appears to play a critical role in providing an efficient channel for the reverse electron transfer (i.e., $S_1 \rightarrow S_0$) in model calculations, as noted in the Introduction. Given the expectation that quantum intramolecular modes play an important role in the electron-transfer process that is being modeled here, an inclusion of quantum intramolecular modes of betaine-30 and how they couple the electronic states of the molecule is necessary. As noted earlier, the MD model that is used here explicitly includes only those intramolecular vibrations associated with relative rotational motions of the rings of the molecule. The remaining degrees of freedom are frozen out by the use of constraints.[57] Further, a quantum mechanical description of the remaining modes is evidently required, based on model calculations.[4,24] A complete quantum mechanical description of the internal modes and their dynamics would require expanding the wave function in eq 10 in internal coordinates q, as

$$|\Phi(\mathbf{R},\mathbf{r},\mathbf{q},\mathbf{t})\rangle = \sum_{I,\alpha} B_{I,\alpha}(t)|\Psi_I(\mathbf{R},\mathbf{r},\mathbf{q})\rangle|\boldsymbol{\xi}_{I,\alpha}(\mathbf{q})\rangle \tag{23}$$

where the total wave function is expanded in internal vibrational state basis functions in addition to the electronic basis functions. The expressions that result from substitution into the time-dependent Schrödinger equation are given in ref 58. Such a scheme is complex because of the large number of coupled equations that result, and additional approximations are highly desirable to put the equations in a form tractable for the present purposes. Here, we focus on incorporation of the additional NA coupling that arises due to the intramolecular quantum degrees of freedom.

We begin with the NA coupling between two electronic state I and J given by the matrix element of the nuclear kinetic energy operator. Conventionally, in mixed quantum classical simulations, the semiclassical expression for this matrix element is used, as given in eqs 11 and 15,

$$V_{IJ} = -i\hbar\dot{\mathbf{R}}\cdot\mathbf{d}_{IJ} \tag{24}$$

This form suffices for the coupling due to the solvent degrees of freedom and the internal relative ring rotations. Here, we add the remaining NA coupling due to the intramolecular degrees of freedom a posterio to the equations of motion for the electronic basis state expansion such that for given vibronic states,

$$i\hbar\dot{\tilde{B}}_I = \tilde{\mathrm{B}}_I E^I_{\mathrm{CI}} - i\hbar\sum_J \tilde{B}_J\left(\dot{\mathbf{R}}\cdot\mathbf{d}_{IJ} - \frac{V^{qm}_{IJ}}{i\hbar}\right) \tag{25}$$

where the additional coupling has the form

$$\begin{aligned}V^{qm}_{IJ} &= \left\langle \Psi_I \middle| \left\langle \alpha_I \middle| \sum_n^{3N-6} -\frac{\hbar^2}{2}\frac{\partial^2}{\partial \mathrm{q}_n{}^2} \middle| \beta_J \right\rangle \middle| \Psi_J \right\rangle \\ &\approx \sum_n^{3N-6} -\hbar^2 \left\langle \Psi_I \middle| \frac{\partial}{\partial q_n} \middle| \Psi_J \right\rangle \left\langle \alpha_I \middle| \frac{\partial}{\partial q_n} \middle| \beta_J \right\rangle\end{aligned} \tag{26}$$

where $|\beta_J\rangle$ and $|\alpha_I\rangle$ are the nuclear wave functions associated with the initial I th and final Jth electronic state, respectively. The kinetic energy operator has been written here in terms of the $3N - 6$ normal modes of the betaine-30 molecule and the second derivative terms due to the nuclear degrees of freedom have been neglected in the second part of eq 26. We assume that the intramolecular nuclear wave function is a direct product of harmonic oscillator wave functions corresponding to the $3N - 6$ internal normal modes of the molecule; that is,

$$|\beta_J\rangle = |\beta^1_J\rangle|\beta^2_J\rangle|\beta^3_J\rangle \cdots |\beta^{3N-6}_J\rangle \tag{27}$$

$\langle\Psi_I|\partial/\partial q_n|\Psi_J\rangle$ is the electronic NA coupling associated with the nth normal mode and the nuclear coupling term $\langle\alpha_I|\partial/\partial q_n|\beta_J\rangle$ factors into

$$\left\langle \alpha_I \middle| \frac{\partial}{\partial q_n} \middle| \beta_J \right\rangle = \left\langle \alpha^n_I \middle| \frac{\partial}{\partial q_n} \middle| \beta^n_J \right\rangle \prod_{m \neq n}^{3N-6} \langle \alpha^m_I | \beta^m_J \rangle \tag{28}$$

In a full treatment, we should evaluate the evolution in eq 25 via a sum over all possible channels, with evaluation of the Franck−Condon factors (eq 28) and appropriate account of the energies of each channel through $\tilde{B}$ (cf. eq 14). To do this in an effective manner requires a relatively thorough analysis, identifying the active vibrational modes and their appropriate parametrization in a harmonic model. Such an analysis, with connection to closely related experimental resonance Raman data,[42] is not undertaken here. Rather, in the present work, we make a very rough approximation that allows us to carry out an initial exploration of the coupling due to the high-frequency modes. Here, we assume that the minima of the internal normal modes of the molecule have the same frequencies in the Ith and Jth electronic state, and are, further, *not* displaced. Under this approximation, the individual nuclear NA coupling matrix elements correspond only to single quanta changes and the Franck−Condon factors are either unity or zero so that

$$\left\langle \alpha_I \middle| \frac{\partial}{\partial q_n} \middle| \beta_J \right\rangle = \frac{1}{\hbar}\sqrt{\frac{\hbar\omega_n}{2}} \tag{29}$$

The electronic NA coupling associated with the *j*th normal mode can be found using the linear transformation coefficients $\{l\}$ between the Cartesian displacement coordinates and the normal modes:

$$\left\langle \Psi_I \left| \frac{\partial}{\partial q_j} \right| \Psi_J \right\rangle = \sum_i^{3N} \frac{(l^{-1})_j^i}{\sqrt{m_i}} \left\langle \Psi_I \left| \frac{\partial}{\partial R_i} \right| \Psi_J \right\rangle \tag{30}$$

where the normal modes are given in terms of the Cartesian displacements of the atoms from their equilibrium positions in mass weighted coordinates,

$$q_i = \sum_j^{3N} l_j^i \sqrt{m_j} \Delta R_j^0 \tag{31}$$

The inclusion of the quantum intramolecular contribution to the NA coupling necessitates a modification of the PPP model for betaine-30 in order to account for the distance dependence of the semiempirical π-electron overlap integral, β. The details of this modification are outlined in Appendix E.

The sets of eigenfrequencies $\{\omega\}$ and normal mode transformation coefficients $\{l\}$ for betaine-30 were calculated from an optimized ground-state geometry with MOPAC 6.0[59] using the AM1 Hamiltonian. The calculation of the displacements along the normal coordinates in eq 31 are made with respect to the minimum energy geometry of the molecule in the reference frame in which the normal modes were calculated:

$$\Delta \mathbf{R}_{\mathrm{B30}}^0 = \mathbf{R}_{\mathrm{B30}} - \mathbf{R}_{\mathrm{B30}}^0 \tag{32}$$

where $\mathbf{R}_{\mathrm{B30}}$ is the vector of the betaine-30 atomic positions and $\mathbf{R}_{\mathrm{B30}}^0$ is the minimum energy reference geometry at which the eigenvalues were calculated. The electronic NA coupling elements $\langle \Psi_I | \partial/\partial q_i | \Psi_J \rangle$ can be strongly dependent on the relative rotational orientation of the molecule with respect to the reference geometry of the molecule.[60] To remove this dependence of the electronic NA coupling elements on overall rotations, the positions, $\mathbf{R}_{\mathrm{B30}}$, and Cartesian elements, $\langle \Psi_I | \partial/\partial R_i | \Psi_J \rangle$, must be expressed in a coordinate system that obeys the Eckart conditions.[60−62] This corresponds to applying an overall translation and rotation to the positions, $\mathbf{R}_{\mathrm{B30}}$, and elements $\langle \Psi_I | \partial/\partial R_i | \Psi_J \rangle$ such that the displacements in the six normal modes corresponding to translation and overall rotation are zero. That is,

$$q_j = \sum_i^{3N} l_i^j \sqrt{m_i} \Delta R_i^0 = 0 \quad \text{for} \quad j = 3N-5, 3N-4, ..., 3N \tag{33}$$

Details for this procedure are outlined in Appendix C.

Having established the details of the equations of motion for the expansion coefficients given by eq 25, we now outline the MDQT algorithm and modifications that must be made to it for the MD model of betaine-30. The equations of motion for the expansion coefficients $\{\tilde{B}\}$ must be integrated in tandem with the propagation of the MD trajectory for the nuclei. These were integrated from molecular dynamics time step t to the next time step $t + \mathrm{d}t$ using a fourth-order Runge−Kutta scheme. Because of the highly oscillatory nature of the coefficients, a much smaller time step was used to integrate eq 25; we use $\delta t = dt/1000$. The computational expense of the calculation of the electronic NA coupling matrix elements precludes calculation of these elements at every one of the smaller time steps. As in previous implementations,[63] these slowly varying coupling elements were linearly interpolated between MD time steps in the integration of the coefficients.

In the fewest switches algorithm,[46] the probability of a transition occurring between t and $t + \mathrm{d}t$ from state K to I can be shown to be

$$P_{K\to I} = \frac{\int_t^{t+dt} \mathrm{d}t\, b_{IK}(t)}{\tilde{B}^*{}_K(t)\, \tilde{\mathrm{B}}_{\mathrm{K}}(t)}. \tag{34}$$

where

$$b_{IK}(t) = -2\mathrm{Re}[\tilde{B}_I(t)\tilde{B}^*{}_K(t)\dot{\mathbf{R}}\cdot\mathbf{d}_{IK}(t)] + 2\hbar^{-1}\mathrm{Im}[\tilde{B}_I(t)\tilde{B}^*{}_K(t)V_{IK}^{qm}(t)] \tag{35}$$

The integration of $b_{IK}(t)$ was done numerically again using linear interpolation for $\dot{\mathbf{R}}\cdot\mathbf{d}_{IK}(t)$ and $V_{IK}^{qm}(t)$. Transitions between states are determined stochastically, based on the state-to-state transition probabilities.

Although it turns out that it does not play an important role in the present results, we also discuss the algorithm for energy conservation when making a transition from one state to another. In this circumstance, the MDQT procedure is to adjust the velocities of the classical nuclei in order to maintain energy conservation. This is done by adjusting the velocity components of the nuclei along the NA coupling vector $\mathbf{d}_{IK}(t)$. However, the velocities are also subject to constraints forces which keep the betaine-30 and solvent molecules rigid. The additional forces that arise from an electronic transition must be adjusted to account for these constraints. Therefore, constraints must be applied to adapt the NA coupling vector so that the changes in velocities are orthogonal to the internal degrees of freedom that are constrained. The method for this is outlined in Appendix D. Once this is done, the velocities of the molecules can be adjusted as follows:

$$\dot{\mathbf{R}}_i = \dot{\mathbf{R}}'_i - \gamma_{KI}\tilde{\mathbf{d}}_{IK}^i/m_i \tag{36}$$

where $\dot{\mathbf{R}}_i'$ is the Cartesian velocity vector of the site i with mass m_i prior to the transition and $\tilde{\boldsymbol{d}}_{IK}^i$ is the adjusted NA coupling vector component for the site i. The scaling factor γ_{KI} is given by[63]

$$\gamma_{IK} = \frac{b_{IK} \pm \sqrt{b_{IK}{}^2 + 4a_{IK}(E_{\mathrm{CI}}^K - E_{\mathrm{CI}}^I)}}{2a_{IK}} \tag{37}$$

where

$$a_{IK} = \sum_i \frac{|\tilde{\mathbf{d}}_{IK}^i|^2}{2m_i} \tag{38}$$

and

$$b_{IK} = \dot{\mathbf{R}}\cdot\tilde{\mathbf{d}}_{IK} \tag{39}$$

The positive root for γ_{IK} is used for $b_{IK} > 0$ and the negative for $b_{IK} < 0$. A transition can occur if γ_{IK} is real. If the particle velocities have insufficient velocity components along $\tilde{\mathbf{d}}_{IK}^i$, then the system does not make a switch and the velocity components of $\dot{\mathbf{R}}$ along $\tilde{\mathbf{d}}_{IK}^i$ are reversed using eq 36 and

$$\gamma_{IK} = \frac{b_{IK}}{a_{IK}} \tag{40}$$

Simulation Details. Simulation details of the MD model used here are described elsewhere[43] and will only be summarized. Simulations were run with a total of 1172 acetonitrile molecules at room temperature and a solvent density of 0.7867 g/cm^3. To simulate the nonequilibrium process of photoexcitation and subsequent relaxation, the MD trajectories were run by placing the betaine-30 molecule in an excited state after the molecule and solvent had been equilibrated in the ground state. The subsequent excited state dynamics were generated with a time step of 2 fs. For computational efficiency, the dynamics was generated using only 50 single excitation configurations to generate the excited-state energies and forces. These 50 were chosen at every MD time step by selecting the 50 lowest energy diagonal elements of the CI matrix defined by eq 1. These 50 lowest energy single excitation states were then used in diagonalization to generate the excited-state energies and molecular forces. It was verified that the ground-state absorption spectrum for the three lowest energy transitions remained unchanged when compared to the spectrum generated using all possible single excitations. This indicated that the wave functions used for the three lowest energy states were well-described by the 50 lowest energy configurations within the space of single excitations. Two types of trajectories were generated. In the first type, of primary interest here, the betaine-30 was placed in the first excited state. In the second type, the betaine-30 was placed in the third excited state. The latter was done to explore the dynamics corresponding to photoexcitation experiments[22] that use excitation wavelengths of both 800 and 400 nm which correspond to the $S_0 \rightarrow S_1$ and $S_0 \rightarrow S_3$ transitions in the experimental absorption spectrum.

III. Results

For this exploratory study, we have examined five trajectories initiated in the S_1 level of betaine-30. We have found that the insight obtained from alternative trajectories is equivalent, and therefore, below, we primarily discuss the results with reference to a particular representative trajectory. To gain an understanding of the details of the relaxation processes that occur after initial excitation of the betaine-30, we first examine the energetics and molecular details of individual trajectories.

The energies of the individual electronic states are shown in Figure 2 as a function of time after the betaine-30 has been placed in the first excited state. The electronic energies of the states are defined as (see section II)

$$E_{S_I} = E_{\mathrm{CI}}^I + V_\pi + V_{\mathrm{C-C}} + V_{\mathrm{C-S}} \quad I = 1, 2, ... \tag{41}$$

We note at the outset that evidence from comparison of experimental and calculated results[43] indicates that the ordering of the S_2 and S_3 states from the present electronic description are reversed, a result that can be seen from their polarities. As will be evident below, the S_2 and S_3 states are computed to be relatively close in energy, with the S_0 and S_1 states well separated from them. Therfore, we focus the present work on the S_0 and S_1 states.

As can be seen from Figure 2, the betaine-30 remains in the first excited state for the 25 ps of the trajectory shown, as discussed below. Examining Figure 2, it can be seen that, immediately after excitation, the S_0 state moves rapidly upward by approximately 1 eV in energy over the first 100 fs of the trajectory. The highest frequency fluctuations in the energy levels are correlated with each other and have a small amplitude of approximately 0.2 eV. Superimposed on the highest frequency fluctuations is a larger amplitude variation of much lower frequency. The low-frequency motion is more pronounced in the S_0 ground-state level (amplitude ~1 eV). The same features can also be seen in the trajectory of the transition energies which are shown in Figure 3. The transition energies are the energy gaps between ground and excited states which are given by $\Delta E_{S_I} = E_{S_I} - E_{S_0} = E_{\mathrm{CI}}^I$ where

$$E_{S_0} = V_\pi + V_{\mathrm{C-C}} + V_{\mathrm{C-S}} \tag{42}$$

To ascertain the connection between specific molecular degrees of freedom and the excitation energies of the betaine-30, we first examine how the torsional angles of the molecule change after excitation. The torsional ring angles as a function of time are plotted in Figure 4. Our previous *ground state* simulation results for betaine-30 in acetonitrile[43] have shown that, in that case, the torsional angles of the molecule only sample a narrow range of angles (±4−8°), indicating that the rings are confined to rotational potential energy wells by barriers much larger than thermal energies. Figure 4 shows the ring angle trajectories for the central ring angle (labeled θ in Figure 1), the two phenyl rings attached to the pyridinium (ϕ in Figure 1), the torsional angles subtended by the phenyl ring ortho to the nitrogen in the pyridinium (χ), and the remaining angle for the two phenyl rings attached to the phenolate group (ξ). As can be seen from Figure 4, the ring angles χ and ξ show no appreciable change from the range of angles that are sampled in the ground state. Further, it is clear that we need not distinguish between the individual angles in pairs of angles ϕ and ξ. However, the central ring angle θ and the two side ring angles ϕ do show considerable deviation from the distributions that they sample in the ground state[43] ($\langle\theta\rangle = 53° \pm 4°$ and $\langle\phi\rangle = 47° \pm 4°$, where the ± denotes the distribution width at half-height).

After excitation, the central ring angle both increases and samples a larger range between 60° and 90°. In addition, the side ring angle motion is correlated with the central ring, and the side angles both increase as the central ring moves toward 90°. The motion of the central ring angle is readily determined to be strongly correlated with the low-frequency large-amplitude motion of the $S_0 \rightarrow S_1$ energy gap (cf. Figure 3 and Figure 4). As the central ring angle opens, the energy gap generally decreases in value, as can be seen by comparing the first 5 ps of the trajectory, shown as a separate frame in both Figures 3 and 4. The overall motion of the energy gaps is clearly correlated with the changes in the central ring angle, with the transition energies getting lower as the pyridinium and phenolate rings approach 90° with respect to each other.

This behavior can be explained by an examination of the calculated potential energy surfaces of the S_0 and S_1 states in the *gas* phase. The gas-phase surfaces shown in Figure 5 were generated as a function of the two ring angles ϕ and θ. These reduced surfaces were each found by first finding the minimum energy structure of the molecule in the gas phase via a simulated annealing MD calculation. The surfaces were then generated by varying only the two angles ϕ and θ and keeping the other angles constrained at their gas-phase minimum energy values; the two ϕ angles were kept equal to each other. In the ground state these two torsional angles have minimum energy values which are 52° and 49°, respectively. At a torsional angle of 0°, the π conjugation between the rings is maximized, but 90° minimizes the steric repulsion between the pendant rings. The $S_0 \rightarrow S_1$ excitation involves the promotion of an electron from

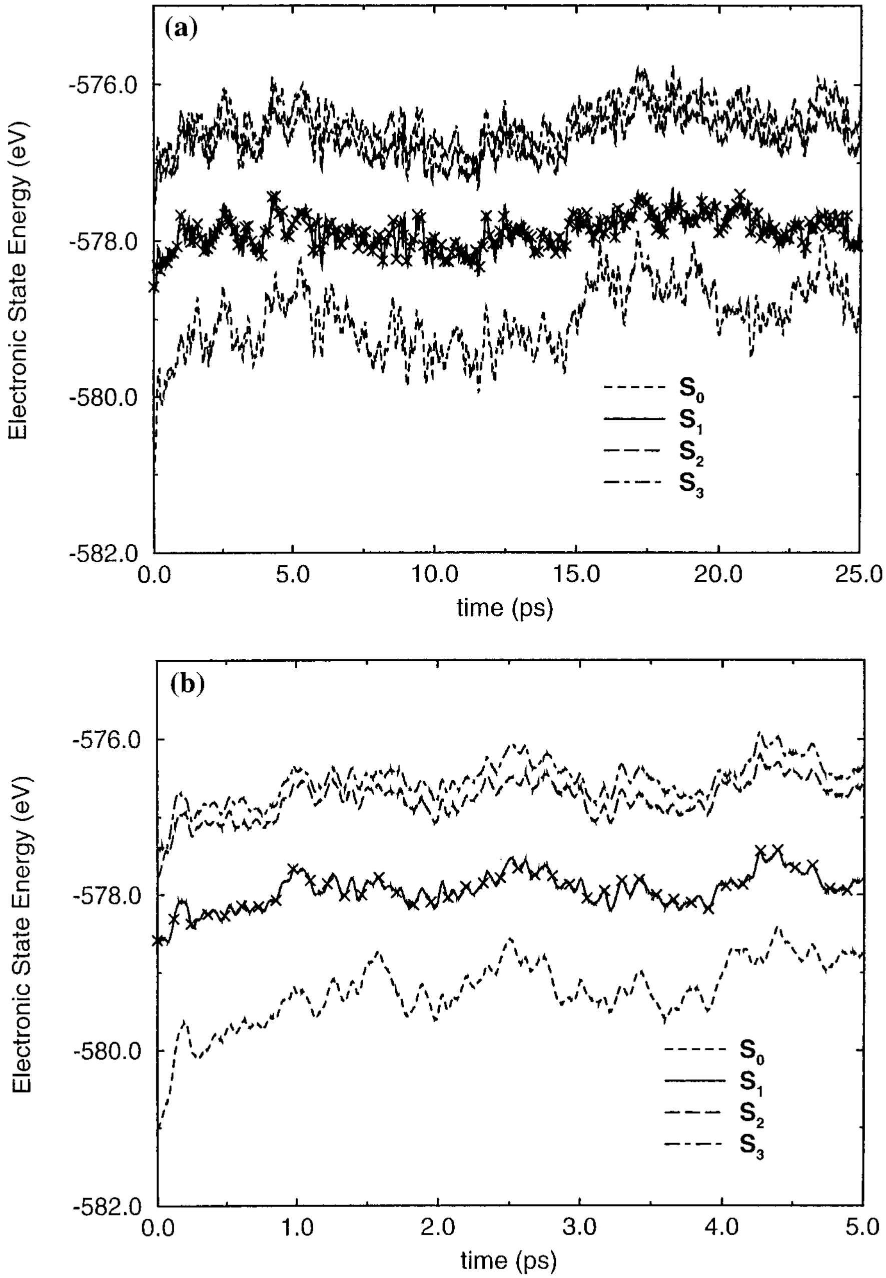

Figure 2. Time-dependent dynamics of the energy levels (see eqs 41 and 42) of betaine-30 after it has been placed in the first excited state S_1 for a typical trajectory. The occupied state is denoted by the crosses. The ground state, S_0, is denoted by the dashed line. The excited states, S_1, S_2, and S_3, are denoted by the solid, long dashed, and dot−dashed lines, respectively. The two frames differ only in the time scale.

a π orbital to a π^* antibonding orbital. This is found to decrease the amount of π conjugation energy in the molecule. For the central ring angle θ, this results in the potential energy minimum being shifted close to $\theta = 90°$, where steric effects are minimized. It is interesting to note that, in the ring angle trajectories, large-amplitude motions occur in the ϕ angles when $\theta \approx 90°$. This is due to the fact that S_1 potential surface is very flat along the ϕ coordinate along the $\theta \approx 90°$ cut, as is evident from Figure 5. The decrease in the transition energies after excitation is also explained by Figure 5; the energy gap is considerably smaller when $\theta \approx 90°$.

While the gas-phase surfaces can be used to interpret the solution state dynamics after excitation, it should be emphasized that there is considerable polarization of this surface by the electric field of the solvent. This is evidenced by the fact that the maximum in the $S_0 \rightarrow S_1$ transition energy in the gas phase is shifted from approximately 29 to 50 kcal/mol, with the solvent increasing the separation of the surfaces shown in Figure 5. Furthermore, our previous simulation results of betaine-30 in the ground state[43] have shown that the solvent polarization substantially removes the θ torsional angle dependence of the $S_0 \rightarrow S_1$ transition energy in the vicinity of the ground state minimum, where the torsional ring angles only sample a very narrow distribution of angles. Conversely, the excited-state trajectories show a dependence of the transition energies on the central ring angle, a result that may be due in part to the much larger range of angles that are sampled in the excited-state trajectory and in part to the rather different solvent polarization present in that case.

We now consider the shorter time dynamics. In Figure 3, a rapid 1 eV drop in the $S_0 \rightarrow S_1$ transition energy is seen which takes place in the first 100−200 fs of the trajectory. This rapid drop in transition energy takes place on a time scale faster than any torsional motion in the betaine-30 molecule and is neces-

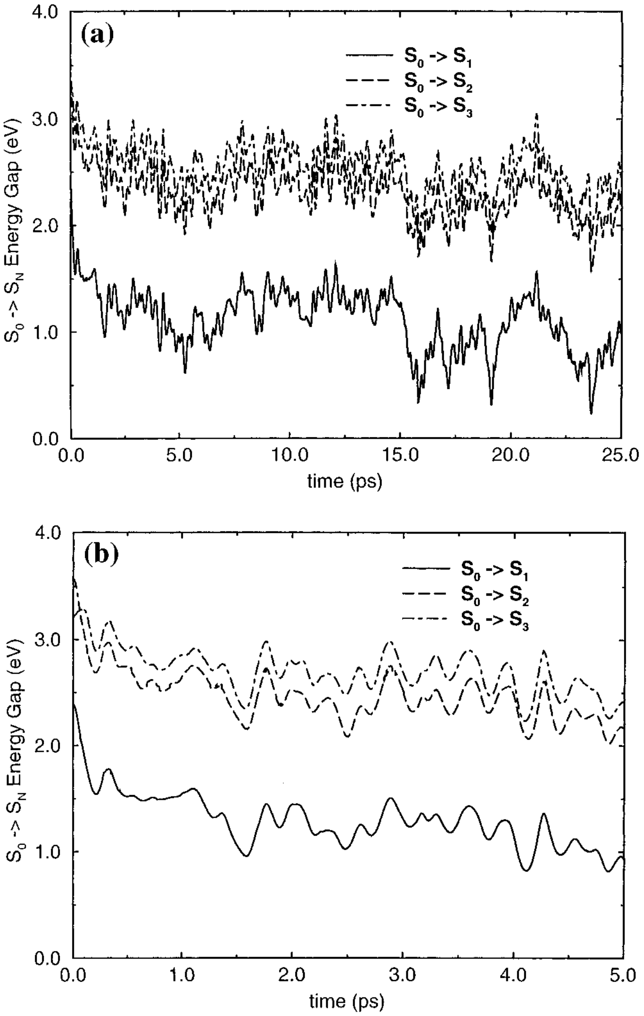

Figure 3. Time-dependent dynamics of the energy gaps $\Delta E_{S_I} = E_{S_I} - E_{S_0}$ of betaine-30 after it has been placed in the first excited state. The energy gaps ΔE_{S_1}, ΔE_{S_2}, and ΔE_{S_3} are denoted by the solid, long dashed, and dot−dashed lines. The trajectory is the same as that shown in Figure 2.

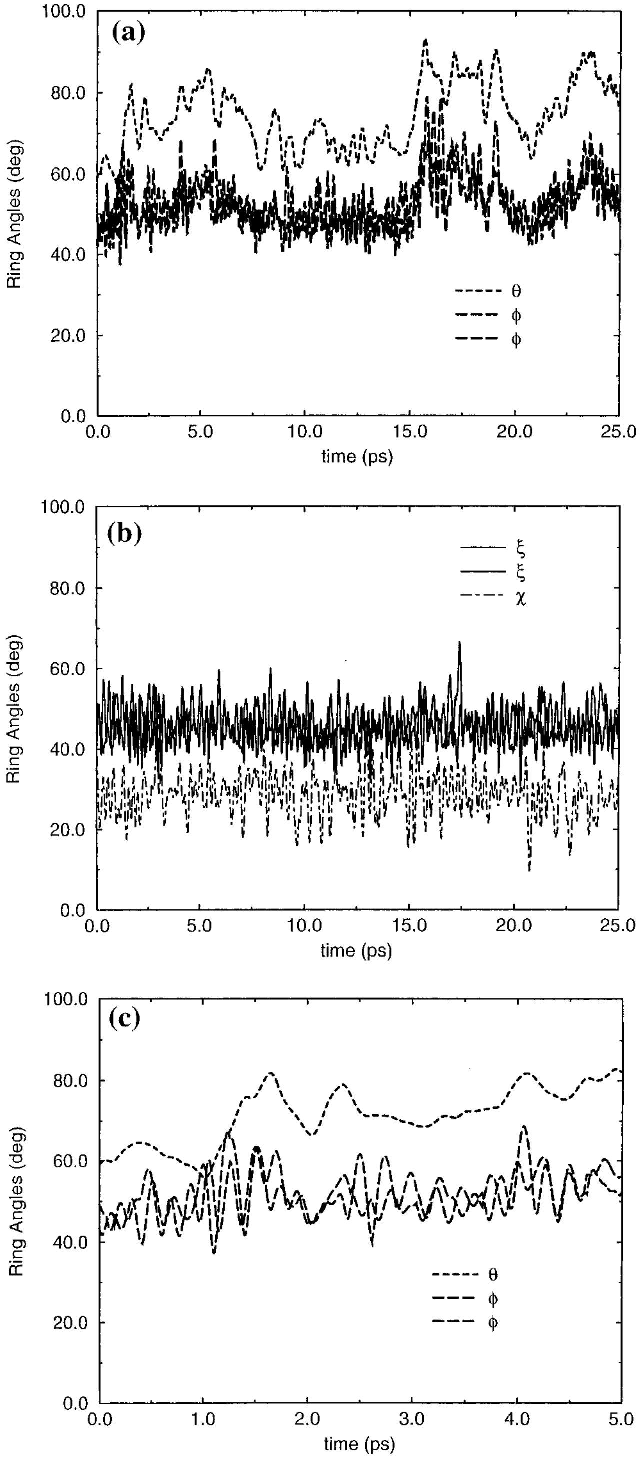

Figure 4. Dynamics of the torsional ring angles of betaine-30 after the system has been excited to the S_1 state at $t = 0$. The labeling of the various angles is given in Figure 1. The trajectory is the same as that shown in Figure 2.

sarily due to solvent motion. This rapid drop immediately after excitation has been seen in many other contexts, both in MD simulations[34−36] and in experiments.[30−33] It occurs due to the rapid inertial motion of the solvent molecules, subject to the different forces present on the two electronic surfaces. The energy gap initially exhibits a Gaussian time dependence as has been shown by MD simulations[36] and molecular theories.[37−40] Longer time solvent dynamics also occurs on a subpicosecond time scale, followed by relaxation dominated by intramolecular torsional motion. It is interesting to note here that the solvent contribution to the energy gap is associated *exclusively* with a rapid rise in the S_0 energy level. This is consistent with the fact that the S_0 state is a charge separated state with a large dipole moment while the S_1 has a much smaller dipole moment.

It is of considerable interest to examine the energy gap relaxation in more detail and to compare the dynamics exhibited in the present work to that inferred from recent modeling of resonance Raman spectra for the same system.[42] In particular, it is evident from Figure 3 and our earlier discussion that, here, the energy gap relaxation exhibits (at least) three time scales. The first, of the order of 100 fs, corresponds to the inertial solvent time scale, and represents about 70% of the subpicosecond response in this trajectory. The second time scale, of the order of 0.5 ps, is the diffusive solvent time scale. After about 1 ps, the solvent is essentially completely relaxed. As noted above, however, there is the potential for considerable additional relaxation on a relatively much longer time scale, due to torsional relaxation around the solute's central dihedral angle. The solvent relaxation contributes about 0.8 eV by 1 ps after initial excitation to S_1; the assignment to solvent alone is evident from Figure 4. This energy relaxation would correspond to a Stokes shift of about 6400 cm^{-1} and an inferred solvent reorganization energy of about 3200 cm^{-1}. This value is comparable to the value of about 3600 cm^{-1} inferred by us for the same model by analysis of solvent contributions to *ground*

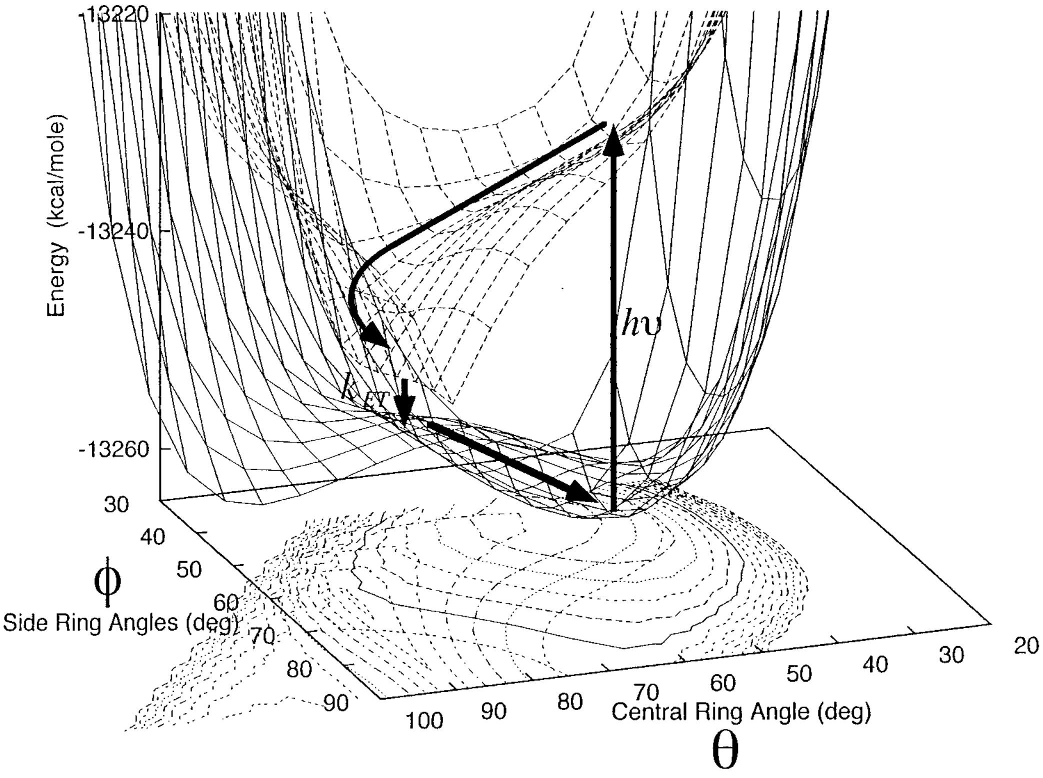

Figure 5. Gas-phase potential energy surfaces for the ground and first excited states as a function of the central phenolate−pyridinium torsion angle θ and the side ring angle ϕ. The minimum of the ground state surface is located at $\theta = 52°$ and $\phi = 49°$. The minimum in the first excited state is shifted to $\theta = 90°$ and $\phi \approx 65°$. The arrows denote the relaxation of the system in these two coordinates after excitation to the first excited state.

state absorption line broadening,[43] a result that also agrees with the corresponding analysis of *experimental* ground-state absorption spectra.[24] The total relaxation accessible including torsional relaxation (observed here due to the long S_1 lifetime of the model) is about 10 000 cm^{-1}.

In the cited resonance Raman spectral modeling, it was found that an ultrafast component of the solvation dynamics was needed to fit the measured results. In particular, McHale and co-workers[42] found that, in addition to a solvation time for acetonitrile of about 0.6 ps, a time of 88 fs carrying an amplitude of about 60% of the solvation response was needed. This form for the solvent response is completely consistent with that seen in the present work. However, the corresponding solvent contribution to the reorganization energy inferred there, about 6000 cm^{-1}, is notably larger than our best estimate[43] of 3600 cm^{-1}. The present observations suggest that a possible factor in the comparison is the role of the slower torsional component observed here. The resonance Raman spectral analysis does not include a slower (classical) intramolecular component so that any effects arising from this would be included in the component attributed to the solvent. These authors[42] have, in fact, suggested the possibility of coupled contributions of solvent with solute torsional degrees of freedom. We note that the torsional relaxation seen here is much slower than the acetonitrile solvent (and also much slower than the ~300 cm^{-1} modes representing the lowest frequencies resolved in the Raman study[42]). Thus, it is not clear without further detailed analysis whether the contribution of the present dihedral motion would be significant in describing the resonance Raman spectra.

As stated earlier, no transition back to the ground state in fact occurs in the present S_1 trajectories. The calculated transition probabilities were found to be extremely low, on the order of $P_{1\to 0} \approx 1 \times 10^{-4}$ per MD time step. A computational study of the estimated lifetime would require averaging over many nonequilibrium trajectories and is not warranted, since the experimental lifetime is known to be approximately 0.5 ps.[24] Alternatively, a first-order lifetime can be estimated from an accumulated transition probability expression

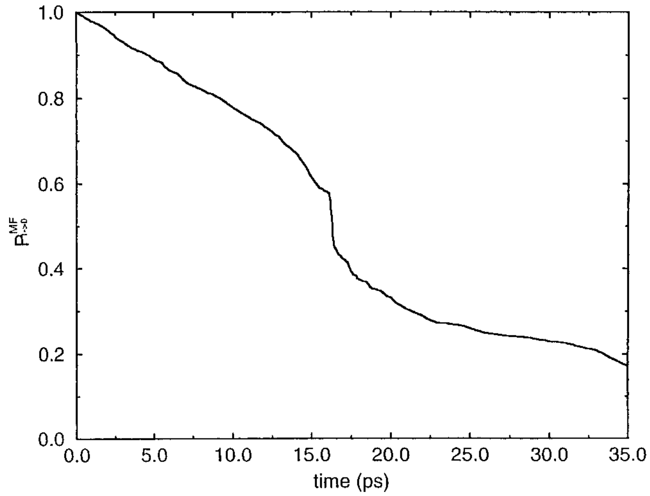

Figure 6. Graph of the accumulated transition probability as given in eq 43 for the trajectory shown in Figure 2.

$$P^{\mathrm{MF}}_{1\to 0} = \prod_{i}^{n_s} (1 - P^{i}_{1\to 0}) \qquad (43)$$

where $P^{i}_{1\to 0}$ is the transition probability at every time MD step which is accumulated over n_s time steps. A graph of $P^{\mathrm{MF}}_{1\to 0}$ as a function of trajectory length for the above trajectory is shown in Figure 6. A linear fit to $\ln[P^{\mathrm{MF}}_{1\to 0}]$ gives an estimate of the excited-state lifetime. The slopes of five trajectories were

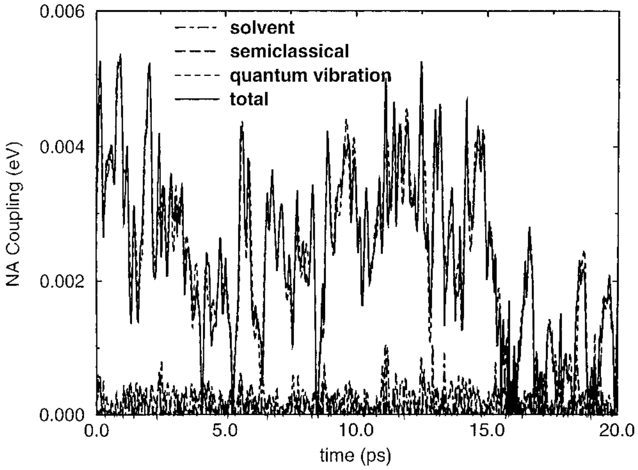

Figure 7. Time dependence of the various contributions to the NA coupling between the ground and first excited states of betaine-30. The solvent contribution to the NA coupling (the first term of eq 44) is given by the dot−dashed line. The semiclassical contribution from the betaine-30 degrees of freedom (the second term of eq 44) is given by the long dashed line. The contribution from the betaine-30 intramolecular vibrational degrees of freedom which has been estimated quantum mechanically (the final term of eq 44) is given by the dashed line. The trajectory is the same as that shown in Figure 2.

averaged to give an estimated lifetime of $\tau_{1\rightarrow 0} = 29 \pm 19$ ps. Clearly, this value is much larger than the experimentally inferred subpicosecond result. It is reasonable to attribute this difference to the relatively crude modeling of the intramolecular vibrational contribution to the transition amplitude used here, since all other aspects are treated much more completely. Among other things, this limits vibrational transitions to $\Delta v = 1$ so that the higher lying vibrational states of the product cannot be accessed from low lying vibrational states of S_1. To explore this interpretation in more detail, we need to examine the separate contributions to the NA coupling from alternative sources, which we do below.

The total NA coupling between the electronic states is given by

$$V_{IJ} = -i\hbar(\dot{\mathbf{R}}^{\mathrm{Sol}}\cdot\mathbf{d}_{IJ}^{\mathrm{Sol}} + \dot{\mathbf{R}}^{\mathrm{B30}}\cdot\mathbf{d}_{IJ}^{\mathrm{B30}}) + V_{IJ}^{\mathrm{qm}} \qquad (44)$$

where, here, the semiclassical contribution to the NA coupling, $\dot{\mathbf{R}}\cdot\mathbf{d}_{IJ}$, has been subdivided into the portions coming from the solvent degrees of freedom and the betaine-30 nuclear degrees of freedom. Because of the fact that internal vibrations in the acetonitrile molecules are rigidly constrained, the only contribution from the solvent degrees of freedom to the NA coupling comes from the intermolecular rotational and translational degrees of freedom of the solvent molecules. Similarly constraints to the motion of the betaine-30 limit the semiclassical contribution to the coupling to that from internal torsional ring motion of the betaine-30. All the other intramolecular degrees of freedom of the betaine-30 contribute to the NA coupling quantum mechanically through the third term in the above equation. We note that the NA coupling from the torsional degrees of freedom is counted twice in the above formulation, but as will be seen below, the contribution from the torsional degrees of freedom is minimal and therefore correction for this is not warranted.

The magnitude of the total NA coupling between the ground and first excited state, $|V_{10}|$, and it's three components are graphed as a function of time in Figure 7 for the trajectory considered in the other figures. As can be seen from the figure, the total NA coupling is determined almost completely by the quantum intramolecular contribution. The semiclassical contributions from the betaine-30 and solvent degrees of freedom are both approximately an order of magnitude smaller than the quantum intramolecular part. The implication of this is that, within the context of the adiabatic reference point of the model presented here, the coupling between S_0 and S_1 that promotes the transition can be well approximated by the contribution due to intramolecular modes. Correspondingly, these modes are the primary recipients of the electronic energy during the NA transition, in accord with the prevailing view discussed in the Introduction. Of course, the observations made here do not imply that the dynamics of the other modes, including both solvent and ring motions, are not critical to the lifetime. The premise of several of the models discussed in the Introduction[4,24,27,28] is that the time-dependent energy gap between electronic states determines the particular vibrational product channels that are potentially activationless and thus most active in the transition. Correspondingly, the rate is modulated by the Franck−Condon factors associated with these states. The present model is unable to address this aspect; this will require a more realistic description of mode displacements.

The contributions to the NA coupling between the various states was also further broken down by the contribution made from each normal mode. First, it was found that the majority (>80%) of the coupling was determined primarily by less than 10 distinct normal modes. Furthermore, the character of these normal modes was high frequency (>600 cm^{-1}), and, consistently, none of the modes included the low-frequency rotational ring torsional modes of the molecule. It is worth noting in this context that resonance Raman studies for the same system[42] reveal a comparable number of active modes and that these cover a similar range of frequencies, although two lower frequency (~300 cm^{-1}) modes of relatively high displacement were also identified in the Raman context. Further analysis of the character of the active modes and how they contribute to the NA coupling is clearly a key subject for future analysis.

To examine the generality of the behaviors discussed above, we have also executed a trajectory initiated in the third excited state of our model. As noted earlier, this state appears to correspond electronically to the S_2, rather than S_3, state so that we do not focus on the details of the results here. However, ultrafast pump−probe experiments have been reported for the excitation of ground-state molecules at 400 nm, which corresponds to a $S_0 \rightarrow S_3$ excitation.[22] One of the main experimental results from this study was that the spectral dynamics for excitation at 800 nm (which corresponds to $S_0 \rightarrow S_1$) were indistinguishable from those that resulted from excitation at 400 nm. The interpretation attached to this result was that internal conversion from $S_3 \rightarrow S_1$ was extremely rapid (<200 fs), followed by the $S_0 \rightarrow S_1$ transition process. For the third excited state in our simulations, with considerably smaller energy gaps between excited states, we do find that the system reaches the S_1 state in less than 500 fs. As for initiation on the S_1 state, the NA coupling is completely dominated by the intramolecular vibrational component. However, the coupling matrix elements are found to be 1−2 orders of magnitude larger than those for the $S_1 \rightarrow S_0$ transition. Thus, we find that these simulation results are consistent with the very short residence times in higher excited states that were inferred experimentally.

IV. Conclusions

The excited state dynamics of betaine-30 in acetonitrile at room temperature has been studied using combined quantum and classical MD simulations. The π electronic degrees of freedom of the betaine-30 have been treated quantum mechanically using the semiempirical PPP electronic structure method,[47−49,64] including perturbation by the solvent. Methods for carrying out time-dependent dynamics, including transitions between molecular electronic states of the molecule have been introduced using the MDQT algorithm[46] suitably modified for the PPP method and the internal geometric constraints of the solute molecule and solvent. An approximate quantum mechanical estimate of the nonadiabatic coupling between the electronic states due to the internal modes of betaine-30 has been used. This estimate does not take into account normal mode displacements between states.

Exploratory simulations reveal that excitation from S_0 to the first excited-state S_1 leads to energy level dynamics that are governed by both the solvent and internal torsional angles of the molecule. The initial response of the energy gap between S_0 and S_1 is governed by the motion of the solvent, with amplitudes and subpicosecond time scales that are consistent with many earlier studies of solvation dynamics in acetonitrile and with resonance Raman studies of betaine-30 in acetonitrile.[42] However, a slower subsequent dynamics of the energy levels and gaps is governed by the internal central phenolate−pyridinium torsional angle of the molecule. This further energy gap relaxation in the first few picoseconds following excitation is substantial, amounting to about 50% of that due to the solvent response. In the S_1 state, the central rings of the molecule rotate toward a geometry where they are perpendicular to each other and sample a much wider distribution of angles than they do in the ground state. This is due both to steric effects and a decreased π conjugation energy in the excited state.

Although the possible role of torsional modes has been noted elsewhere,[42] and fast intramolecular classical degrees of freedom have been invoked in modeling,[24] the inclusion of a relatively slow, but large-amplitude, component in the energy gap relaxation has not been addressed in ET modeling of this system. The identification of the specific mode here is also new. It is of considerable interest for future work to determine whether this internal rotation can be associated with those invoked in models and if inclusion of such a degree of freedom can be a benefit to the modeling of resonance Raman spectra. In any case, it would appear from these results that the a priori separation of solvent and intramolecular degrees of freedom from experimental data alone is, at best, very challenging.

While excitation gives rise to a response from the solvent and a change in the internal geometry of the molecule, the nonadiabatic couplings between the electronic states are found to be determined almost exclusively by a small number of high-frequency internal molecular modes of the betaine-30. Because of the very approximate model used for treating these high-frequency modes here, we have not been able to directly address the relative importance of the different solvent dynamical time scales on the back ET rate $S_1 \rightarrow S_0$. With improvements to this aspect of the model, and inclusion of multiple vibronic channels for relaxation, this question can be addressed and closer connection to resonance Raman experiments can be made. This will be the topic of future studies.

Appendix A: Evaluation of Nuclear Derivatives

The coupled perturbed Hartree−Fock (CPHF) equations are given by

$$(\epsilon_p - \epsilon_q)u^R_{qp} = F'_{qp} \tag{A1}$$

where F'_{qp} is given by

$$F'_{qp} = \sum_{\mu\nu} c^q_\mu \frac{\partial F_{\mu\nu}}{\partial R} c^p_\nu \tag{A2}$$

The matrix elements $F_{\mu\nu}$ are the Fock matrix elements in the atomic orbital representation. Using the definitions of the Fock matrix elements for the PPP Hamiltonian given by eq 4 in ref 43, the above equation becomes

$$(\epsilon_p - \epsilon_q)u^R_{qp} = B^R_{qp} + \sum_a^{\text{virtual}} \sum_i^{\text{real}} A_{ai,qp} u^R_{qp} \tag{8}$$

where the matrix **A** can be shown to be

$$A_{ai,qp} = -\frac{1}{2}\sum_{\mu\neq\nu} X^{\mu\nu}_{ai} c^q_\mu c^p_\nu \gamma_{\mu\nu} + \frac{1}{2}\sum_{\mu} X^{\mu\mu}_{ai} c^q_\mu c^p_\mu \gamma_{\mu\mu} + \sum_{\mu\neq\rho} X^{\rho\rho}_{ai} c^q_\mu c^p_\mu \gamma_{\mu\rho} \tag{A3}$$

where

$$X^{\mu\nu}_{ai} = 2(c^i_\mu c^a_\nu + c^a_\mu c^i_\nu) \tag{A4}$$

The vector **B** is given by

$$B^R_{qp} = H'_{qp} - \frac{1}{2}\sum_{\mu\neq\nu} c^q_\mu c^p_\nu \mathrm{P}_{\mu\nu} \gamma^{(R)}_{\mu\nu} + \frac{1}{2}\sum_{\mu} c^q_\mu c^p_\mu P_{\mu\mu} \gamma^{(R)}_{\mu\mu} + \sum_{\mu\neq\rho} c^q_\mu c^p_\mu P_{\rho\rho} \gamma^{(R)}_{\mu\rho} \tag{A5}$$

where

$$H'_{qp} = \sum_{\mu\nu} c^q_\mu \frac{\partial H_{\mu\nu}}{\partial R} c^p_\nu \tag{A6}$$

The matrix elements $H_{\mu\nu}$ are the one-electron Hamiltonian PPP matrix elements,[64] $\mathrm{P}_{\mu\nu}$ is the density matrix defined by $P_{\mu\nu} = 2\sum_i^{\text{real}} c^i_\mu c^i_\nu$.

To avoid explicitly solving the CPHF equations for each nuclear derivative we first rewrite eq 8 in matrix form

$$(\epsilon_{\mathrm{p}} - \epsilon_{\mathrm{q}})u^R_{qp} - \sum_a^{\text{virtual}} \sum_i^{\text{real}} A_{ai,qp} u^R_{qp} = B^R_{qp}$$

$$\mathbf{G}\mathbf{u}^R = \mathbf{B}^R \tag{A7}$$

which can be solved through matrix inversion

$$\mathbf{u}^R = \mathbf{G}^{-1}\mathbf{B}^R \tag{A8}$$

Rewriting eq 7 in matrix notation and substituting eq A8 into 7

$$\sum_{mn} C^I_m C^I_n \frac{\partial}{\partial R} A_{nm} = \sum_{mn} C^I_m C^I_n A^{(R)}_{nm} + 2\boldsymbol{\zeta}^I \mathbf{u}^R$$

$$\sum_{mn} C^I_m C^I_n \frac{\partial}{\partial R} A_{nm} = \sum_{mn} C^I_m C^I_n A^{(R)}_{nm} + 2\boldsymbol{\zeta}^I \mathbf{G}^{-1} \mathbf{B}^R$$

$$\sum_{mn} C^I_m C^I_n \frac{\partial}{\partial R} A_{nm} = \sum_{mn} C^I_m C^I_n A^{(R)}_{nm} + 2\mathbf{Z}_I \mathbf{B}^R \tag{A9}$$

The vector−matrix product $\boldsymbol{\zeta}^I \boldsymbol{G}^{-1} = \mathbf{Z}_I$ need only be evaluated once per CI state, as opposed to $3N$ times (where N is the total number of classical nuclei in the simulation) as it would be if the CPHF equations for $\mathbf{u}^R$ were solved directly for each nuclear coordinate. Since $\mathbf{u}^R$ is no longer solved for directly, the NA coupling vector from eq 22 must now be rewritten in terms of $\mathbf{B}^R$:

$$\left\langle \Psi_I \middle| \frac{\partial}{\partial R} \Psi_J \right\rangle = d_{IJ}^R = \frac{\sum\limits_{mn} C_n^I C_m^J A_{nm}^{(R)}}{(E_{\mathrm{CI}}^J - E_{\mathrm{CI}}^I)} + 2\sum_{ks} u_{ks}^R \zeta_{ks}^{IJ}$$
$$= \frac{\sum\limits_{mn} C_n^I C_m^J A_{nm}^{(R)}}{(E_{\mathrm{CI}}^J - E_{\mathrm{CI}}^I)} + 2\zeta^{IJ}\mathbf{G}^{-1}\mathbf{B}^R \tag{A10}$$
$$= \frac{\sum\limits_{mn} C_n^I C_m^J A_{nm}^{(R)}}{(E_{\mathrm{CI}}^J - E_{\mathrm{CI}}^I)} + 2\mathbf{Z}_{IJ}\mathbf{B}^R$$

The vector−matrix product, $\zeta^{IJ}\mathbf{G}^{-1} = \mathbf{Z}_{IJ}$, is evaluated once for every pair of CI states.

Appendix B: Simplification of Gradient Matrix Elements between Slater Determinants

The simplification of gradient terms of the form $\langle\psi_n|\nabla_R\psi_m\rangle$ can be carried out by recognizing that ∇_R acts as a one electron operator. Therefore, Slater determinants that differ by more than one spin−orbital will be zero, i.e.,

$$\langle\psi_{i\to a}|\nabla_{\boldsymbol{R}}|\psi_{j\to b}\rangle = 0 \tag{B1}$$

The remaining matrix elements for the one-electron excitations and ground-state Slater determinants will be

$$\langle\psi_0|\nabla_R|\psi_0\rangle = \sum_i^{\text{occupied}} \langle i|\nabla_{\boldsymbol{R}}|i\rangle \tag{B2a}$$

$$\langle\psi_{i\to a}|\nabla_R|\psi_{i\to a}\rangle = \sum_j^{\text{occupied}} \langle j|\nabla_R|j\rangle - \langle i|\nabla_R|i\rangle + \langle a|\nabla_R|a\rangle \tag{B2b}$$

$$\langle\psi_{i\to a}|\nabla_R|\psi_0\rangle = \sqrt{2}\langle a|\nabla_R|i\rangle \tag{B2c}$$

$$\langle\psi_{i\to a}|\nabla_R|\psi_{j\to a}\rangle = \sqrt{2}\langle j|\nabla_R|i\rangle \tag{B2d}$$

$$\langle\psi_{i\to a}|\nabla_R|\psi_{i\to b}\rangle = \sqrt{2}\langle a|\nabla_R|b\rangle \tag{B2e}$$

The ket $|i\rangle$ is the state ket for the *i*th real space MO, which is expanded in terms of atomic orbital basis functions

$$|i\rangle = \sum_\mu c_\mu^i |\mu\rangle \tag{B3}$$

There are two types of MO matrix elements in eqs B2a−e, diagonal elements of the type $\langle i|\partial/\partial R|i\rangle$ and off-diagonal elements of the form $\langle i|\partial/\partial R|a\rangle$. Expanding the diagonal elements using (B3), $\langle i|\partial/\partial R|i\rangle$ then become

$$\left\langle i\middle|\frac{\partial}{\partial R}\middle|i\right\rangle = \sum_{\mu\nu} c_\mu^i c_\nu^i \left\langle \mu \middle| \frac{\partial}{\partial \mathrm{R}} \middle| \nu \right\rangle + \sum_{\mu\nu} \langle\mu|\nu\rangle c_\mu^i \frac{\partial c_\nu^i}{\partial R}$$
$$= \sum_{\mu\nu} c_\mu^i c_\nu^i \left\langle \mu \middle| \frac{\partial}{\partial \mathrm{R}} \middle| \nu \right\rangle + \sum_\mu c_\mu^i \frac{\partial c_\mu^i}{\partial R} \tag{B4}$$

Focusing our attention on the first term of eq B4, off-diagonal elements, $\langle\mu|\partial/\partial R|\nu\rangle$, are approximated to be zero under the zero differential overlap approximation (i.e., the orthonormality of the atomic orbital basis functions) which was assumed in the implementation of the PPP method for betaine-30 as outlined in ref 43. Assuming that the atomic orbital basis functions are real, one can show that derivatives of the diagonal matrix elements are zero due to orthonormalilty, i.e.,

$$\frac{\partial}{\partial R}\langle\mu|\mu\rangle = 2\left\langle\mu\middle|\frac{\partial}{\partial R}\mu\right\rangle = 0 \tag{B5}$$

These two results demonstrate that the first term in eq B4 is zero. In a similar fashion, one can show using the orthonormality of the MOs that the second term is zero as well

$$\frac{\partial}{\partial R}\langle i|i\rangle = \sum_{\mu\nu}\langle\mu|\nu\rangle c_\mu^i \frac{\partial c_\nu^i}{\partial R} + \langle\mu|\nu\rangle c_\nu{}^i \frac{\partial c_\mu^i}{\partial R}$$
$$= 2\sum_\mu c_\mu^i \frac{\partial c_\mu^i}{\partial R} = 0 \tag{B6}$$

It can be thus concluded that all diagonal elements of the form $\langle i|\partial/\partial R|i\rangle$ are zero and eqs B2a and B2b are both zero. Off-diagonal elements, however, are not zero and, using the previous results, are given by

$$\left\langle i\middle|\frac{\partial}{\partial R}\middle|a\right\rangle = \sum_\mu c_\mu^i \frac{\partial c_\mu^a}{\partial R} \tag{B7}$$

Hence, one obtains the result shown in eq 21,

$$\langle\psi_{i\to a}|\nabla_R\psi_0\rangle = \sqrt{2}\sum_\mu c_\mu^i \nabla_R c_\mu^a$$
$$\langle\psi_{i\to b}|\nabla_R\psi_{i\to a}\rangle = \sqrt{2}\sum_\mu c_\mu^b \nabla_R c_\mu^a \tag{B8}$$
$$\langle\psi_{i\to a}|\nabla_R\psi_{j\to a}\rangle = \sqrt{2}\sum_\mu c_\mu^j \nabla_R c_\mu^i$$

Appendix C: Compliance with Eckart Conditions

The positions of the atoms of the betaine-30 molecule must be rotated and translated to a reference frame such that only $3N - 6$ of the normal modes of the molecule have finite displacements:

$$q_j = \sum_i^{3N} l_i^j \sqrt{m_i} \Delta R_i^0 = 0 \quad \text{for} \quad j = 3N-5, 3N-4, ..., 3N \tag{C1}$$

The Cartesian displacement vector, $\Delta\mathbf{R}_{\mathrm{B30}}^0$ (whose components are ΔR_i^0 in the above equation), is the difference between the betaine-30 coordinates in the MD simulation at a given time step *after* overall rotation and translation, $\mathbf{R}_{\mathrm{B30}}$, and the coordinates of the molecule in it’s minimum energy gas-phase configuration, $\mathbf{R}^0_{\mathrm{B30}}$, i.e.,

$$\Delta\mathbf{R}^0_{\mathrm{B30}} = \mathbf{R}_{\mathrm{B30}} - \mathbf{R}^0_{\mathrm{B30}} \tag{C2}$$

The normal-mode frequencies and transformation coefficients are, of course, calculated at the configuration $\mathbf{R}^0_{\mathrm{B30}}$. Equation C1 can only be satisfied by choosing the coordinate system such that the positions satisfy the Eckart conditions.[60-62] The first condition is trivially satisfied by making the center of masses coincident with the origin of the coordinate system:

$$\sum_i^N m_i\mathbf{R}_i = \sum_i^N m_i\mathbf{R}_i^0 = 0 \tag{C3}$$

The vectors $\mathbf{R}_i$ and $\mathbf{R}_i^0$ denote the coordinates of the ith betaine-30 atom position in the two respective geometries. The second Eckart conditions correspond to the static equivalent of the angular moment between the two sets of coordinates being zero:

$$\sum_i^N m_i(\mathbf{R}_i \times \mathbf{R}_i^0) = 0 \tag{C4}$$

This condition can be satisfied by applying a suitably chosen rotation matrix, $\mathbf{T}$, to the betaine-30 positions from the MD simulation. The procedure for finding such a rotation matrix is outlined in ref 65 and is not repeated here. With the rotation matrix in hand, the matrix element of the NA coupling in a normal mode coordinate system, $\langle\Psi_I|\partial/\partial q_j|\Psi_J\rangle$, can be found. The notation of eq 30 is changed slightly to clarify the transformation of the Cartesian matrix elements using the rotation matrix

$$\left\langle\Psi_I\left|\frac{\partial}{\partial q_j}\right|\Psi_J\right\rangle = \sum_i^N\sum_k^3 \frac{(l^{-1})_j^{i,k}}{\sqrt{m_k}}\left\langle\Psi_I\left|\frac{\partial}{\partial R_{i,k}}\right|\Psi_J\right\rangle \tag{C5}$$

The Cartesian elements of the NA coupling matrix, $\langle\Psi_I|\partial/\partial R_{i,k}|\Psi_J\rangle$, are calculated after application of the rotation to the betaine-30 positions. The rotation matrix transforms the positions, $\hat{\mathbf{R}}_i$, to ones that satisfy the Eckart conditions:

$$\mathbf{T}\hat{\mathbf{R}}_i = \mathbf{R}_i \tag{C6}$$

Rewriting eq C6,

$$\tilde{\mathbf{T}}\mathbf{R}_i = \hat{\mathbf{R}}_i \tag{C7}$$

one sees that the Cartesian derivatives in eq C5 may be rewritten as

$$\frac{\partial}{\partial R_{i,k}} = \sum_l^3 \frac{\partial\hat{R}_{i,l}}{\partial R_{i,k}}\frac{\partial}{\partial\hat{R}_{i,l}} \tag{C8}$$

Using this relation, the elements, $\langle\Psi_I|\partial/\partial q_i|\Psi_J\rangle$, can now be expressed in terms of the Cartesian NA coupling matrix elements that are found in the MD simulation, $\langle\Psi_I|\partial/\partial\hat{R}_{i,l}|\Psi_J\rangle$:

$$\left\langle\Psi_I\left|\frac{\partial}{\partial q_j}\right|\Psi_J\right\rangle = \sum_i^N\sum_k^3\sum_l^3 \frac{(l^{-1})_j^{i,k}\tilde{T}_{kl}}{\sqrt{m_k}}\left\langle\Psi_I\left|\frac{\partial}{\partial\hat{R}_{i,l}}\right|\Psi_J\right\rangle \tag{C9}$$

Appendix D: Nuclear Velocity Adjustments with Molecular Constraints

Adjusting the nuclear velocities along components parallel to the NA coupling vector $\mathbf{d}^i_{IJ}$ maintains energy conservation when a NA transition occurs. However, the presence of intramolecular constraints means that the NA coupling vector must be adjusted prior to adjusting the velocities by subtracting out the vector components along the derivative of the constraints. This is done by applying constraint conditions in form of Lagrange multipliers to the coupling vector itself. One considers $\mathbf{d}^i_{IJ}/m_i$ for a site i to be a NA force to which a constraint may be applied. Following the method of Ciccotti, Ferrario, and Rycaert,[66] we subdivide the nuclear sites of a molecule into two sets. The first set consists of primary atoms between which distance constraints are applied. The second set is composed of atoms whose positions are expressed as linear combinations of the primary atom positions. There will l_b primary constraints of the form

$$\sigma_P = d_P^2 - |\boldsymbol{R}_i - \boldsymbol{R}_j|^2 = 0 \tag{D1}$$

where d_P is the distance between the sites $\mathbf{R}_i$ and $\mathbf{R}_j$. In practice, these sites need not be primary nuclear positions themselves within the molecule, they can be linear combinations of primary nuclear site positions if an entire group of atoms within the molecule is being treated as a rigid whole, but for the sake of clarity it will be assumed that they represent the primary atomic positions themselves. The constraint conditions on the secondary atoms, of which there will be n_{s}, are given by

$$\boldsymbol{\tau}_\alpha = \sum_{i=1}^{n_b} C_{\alpha i}\mathbf{R}_i - \mathbf{r}_\alpha = 0 \tag{D2}$$

where there are n_b primary sites. The NA force vectors are also divided into primary and secondary groups, to which the constraint conditions using the method of Lagrange multipliers are applied.

$$\frac{\tilde{\mathbf{d}}^i_{IK}}{m_i} = \frac{\mathbf{d}^i_{IK}}{m_i} - \sum_{P=1}^{l_b}\frac{\lambda_P}{m_i}\nabla_i\sigma_P - \sum_{\beta=1}^{n_{\mathrm{s}}}\frac{\nabla_i(\boldsymbol{\mu}_\beta\cdot\boldsymbol{\tau}_\beta)}{m_i} \tag{D3}$$

$$\frac{\tilde{\mathbf{d}}^\alpha_{IK}}{m_\alpha} = \frac{\mathbf{d}^\alpha_{IK}}{m_\alpha} - \sum_{\beta=1}^{n_{\mathrm{s}}}\frac{\nabla_\alpha(\boldsymbol{\mu}_\beta\cdot\boldsymbol{\tau}_\beta)}{m_\alpha} \tag{D4}$$

where λ_P and μ_β are the Lagrange multipliers for the primary and secondary constraint conditions. The adjusted NA coupling vectors $\tilde{\mathbf{d}}^i_{IK}$ and $\tilde{\mathbf{d}}^\alpha_{IK}$ will be used to adjust the velocities as per eq 36. Next, we use the fact that the adjusted NA force vectors for the secondary sites must obey eq D2:

$$\frac{\tilde{\mathbf{d}}^\alpha_{IK}}{m_\alpha} = \sum_{i=1}^{n_b} C_{\alpha i}\frac{\tilde{\mathbf{d}}^i_{IK}}{m_i}. \tag{D5}$$

Using this equation it is possible solve for the secondary Lagrange multipliers, $\boldsymbol{\mu}_\beta$, and show that

$$\tilde{\mathbf{d}}^i_{IK} = p_i - \sum_{P=1}^{l_b}\lambda_P\Delta_{iP} \tag{D6}$$

where

$$\Delta_{iP} = \nabla_i \sigma_P - \sum_{j=1}^{n_b} \sum_{\alpha,\beta=1}^{n_s} C_{\alpha i} A^{-1}_{\alpha\beta} \frac{C_{\beta j}}{m_j} \nabla_j \sigma_P \tag{D7}$$

The matrix **A** is given by

$$A_{\alpha\beta} = \frac{\delta_{\alpha\beta}}{m_\alpha} + \sum_{i=1}^{n_b} \frac{C_{\alpha i} C_{\beta i}}{m_\alpha}. \tag{D8}$$

The first term of eq D6, p_i, is given by

$$p_i = \mathbf{d}^i_{IK} - \sum_{\alpha,\beta=1}^{n_s} C_{\alpha i} A^{-1}_{\alpha\beta} \mathbf{T}_\beta \tag{D9}$$

where

$$\mathbf{T}_\beta = \frac{\mathbf{d}^\beta_{IK}}{m_\beta} + \sum_{i=1}^{n_b} \frac{C_{\beta i} \mathbf{d}^i_{IK}}{m_i}. \tag{D10}$$

Now all that remains to is to find the set Lagrange multipliers for the primary constraints. This can be done taking the equation for the scaled velocities (eq 36) and inserting eq D6 for $\tilde{\mathbf{d}}^i_{IK}$

$$\dot{\mathbf{R}}_i - \dot{\mathbf{R}}'_i = -\frac{\gamma_{IK}}{m_i} p_i + \frac{\gamma_{IK}}{m_i} \sum_{P=1}^{l_b} \lambda_P \Delta_{iP} \tag{D11}$$

We now subtract ($\dot{\mathbf{R}}_j - \dot{\mathbf{R}}'_j$) from both sides of (D11) to obtain

$$\dot{\mathbf{R}}_{ij} - \dot{\mathbf{R}}'_{ij} = -\gamma_{\mathrm{IK}} \left(\frac{p_i}{m_i} - \frac{p_j}{m_j} \right) + \gamma_{IK} \sum_{P=1}^{l_b} \lambda_{\mathrm{P}} \left(\frac{\Delta_{iP}}{m_i} - \frac{\Delta_{jP}}{m_j} \right) \tag{D12}$$

If $\dot{\mathbf{R}}_{ij}$ is the difference in velocities between two sites that have a primary constraint between them, then the dot product of $\dot{\mathbf{R}}_{ij}$ with each term of the left-hand side of eq D12 will be zero, i.e.,

$$\dot{\mathbf{R}}_{ij} \cdot \mathbf{R}_{ij} = \dot{\mathbf{R}}'_{ij} \cdot \mathbf{R}_{ij} = 0 \tag{D13}$$

because the velocities along the derivative of the constraint should be zero both before and after they are adjusted for the NA transition. This implies that there are l_b equations of the form

$$\mathbf{R}_{ij} \cdot \left(\frac{p_i}{m_i} - \frac{p_j}{m_j} \right) = \sum_{P=1}^{l_b} \lambda_P \mathbf{R}_{ij} \cdot \left(\frac{\Delta_{iP}}{m_i} - \frac{\Delta_{jP}}{m_j} \right) \tag{D14}$$

These equations can be rewritten in matrix form

$$\tilde{\mathbf{B}} = \tilde{\mathbf{A}} \boldsymbol{\lambda} \tag{D15}$$

where the vector $\tilde{\mathbf{B}}$ is given by

$$\tilde{\mathbf{B}} = \left(\begin{array}{l} \mathbf{R}_{ij} \cdot \left(\dfrac{p_i}{m_i} - \dfrac{p_j}{m_j} \right) \\ \vdots \\ \mathbf{R}_{kn} \cdot \left(\dfrac{p_k}{m_k} - \dfrac{p_n}{m_n} \right) \end{array} \right) \tag{D16}$$

The matrix $\tilde{\mathbf{A}}$ has elements

$$\tilde{A}_{\mathrm{mn}} = \mathbf{R}_{ij} \cdot \left(\frac{\Delta_{in}}{m_i} - \frac{\Delta_{jn}}{m_j} \right) \tag{D17}$$

where the index m denotes a pair of sites (i,j) that make up the mth constraint. The matrix $\tilde{\mathbf{A}}$ can then be inverted to find the primary Lagrangian constraints. With the constraints in hand the adjusted primary NA coupling vectors $\tilde{\mathbf{d}}^i_{IK}$ can be found from eq D6 and the secondary NA coupling vectors $\tilde{\mathbf{d}}^\alpha_{IK}$ from eq D5.

TABLE 1: Parameters for the Numerical Fit to the Lindberg[67] Equation for the Semiempirical Overlap Integral $\boldsymbol{\beta}_{\mathrm{CX}}$

site X	μ_{CX} (bohr^{-1})	β_1^{CX} (hartrees)	β_2^{CX} (hartrees bohr^{-1})
C	0.67931	−0.083032	0.031686
N	0.80659	−0.074106	0.029008
O	0.89987	−0.095542	0.035262

Appendix E: Distance-Dependent $\boldsymbol{\beta}$ Parameter

In the implementation of the PPP method for betaine-30 in ref 43, the semiempirical π-electron overlap integral β was treated as a constant. This was appropriate since the relative motion between chemically bonded pairs of atoms was constrained. Furthermore, gradient terms of β need not be included in that case for the semiclassical NA coupling term $\mathbf{d}_{\mathrm{IJ}} \cdot \dot{\mathbf{R}}$ in eq 25 because there are no nuclear velocities with components along the bonds of the molecule. However, the gradient of β terms must be included when evaluating the NA coupling matrix elements in eq 25 for the quantum intramolecular contribution to the NA coupling. The overlap integral in our previous implementation was evaluated using the Linderberg approximation:[67]

$$\beta_{\mu\nu} = (\hbar^2/m_{\mathrm{e}}) R^{-1}_{\mu\nu} \frac{\mathrm{d}S_{\mu\nu}}{\mathrm{d}R_{\mu\nu}} \tag{E1}$$

where $\hbar$ is Planck's constant over 2π, m_{e} is the electron mass, and $S_{\mu\nu}$ is the overlap integral between atomic orbitals μ and ν which are separated by the distance $R_{\mu\nu}$. To evaluate eq E1 and its gradients in the calculations, we use a numerical fit to an evaluation of this a priori expression with standard Slater orbital parameters.[68] The fitting expression used is

$$\beta_{\mu\nu} = \exp(-\mu_{\mathrm{CX}}(R_{\mu\nu} - R^{\mathrm{eq}}_{\mathrm{CX}}))[\beta_1^{\mathrm{CX}} + \beta_2^{\mathrm{CX}}(R_{\mu\nu} - R^{\mathrm{eq}}_{\mathrm{CX}})] \tag{E2}$$

The values of the parameters for eq E2 are listed in Table 1.

Acknowledgment. The authors are grateful for support of this research by a grant from the NSF. Partial support of this work by the Texas Advanced Research Program and the Institute for Theoretical Chemistry, University of Texas at Austin is also gratefully acknowledged. J.L. has been supported in part by a postdoctoral fellowship from the Natural Sciences and Engineering Research Council of Canada and by an NSF/CISE Postdoctoral grant (ASC-9704682).

References and Notes

(1) Barbara, P. F.; Meyer, T. J.; Ratner, M. A. *J. Phys. Chem.* **1996**, *100*, 13148.

(2) Sumi, H.; Marcus, R. A. *J. Chem. Phys.* **1986**, *84*, 4894.

(3) Nadler, W.; Marcus, R. A. *J. Chem. Phys.* **1987**, *86*, 3906.

(4) Jortner, J.; Bixon, M. *J. Chem. Phys.* **1988**, *88*, 167.

(5) Alexandrov, I. V. *Chem. Phys.* **1980**, *51*, 449.

(6) Calef, D. F.; Wolynes, P. G. *J. Phys. Chem.* **1983**, *87*, 3387.

(7) Zwan, G. v. d.; Hynes, J. T. *J. Chem. Phys.* **1982**, *76*, 2993.

(8) Zusman, L. D. *Chem. Phys.* **1980**, *49*, 295.

(9) Tominaga, K.; Walker, G. C.; Kang, T. J.; Barbara, P. F. *J. Phys. Chem.* **1991**, *95*, 10485.

(10) Reid, P. J.; Silva, C.; Barbara, P. F.; Karki, L.; Hupp, J. T. *J. Phys. Chem.* **1995**, *99*, 2609.

(11) Reid, P.; Barbara, P. F. *J. Phys. Chem.* **1995**, *99*, 3554.
(12) Yoshihara, K.; Tominaga, K.; Nagasawa, Y. *Bull. Chem. Soc. Jpn.* **1995**, *68*, 696.
(13) Su, S.-G.; Simon, J. D. *J. Phys. Chem.* **1988**, *92*, 2395.
(14) Maroncelli, M.; MacInnis, J.; Fleming, G. R. *Science* **1989**, *243*, 1674.
(15) Reichardt, C. *Angew. Chem., Int. Ed. Engl.* **1979**, *18*, 98.
(16) Reichardt, C. *Solvents and Solvent Effects in Organic Chemistry*; Weinheim: New York, 1988.
(17) Plieninger, P.; Baumgärtel, H. *Ber. Bunsen-Ges. Phys. Chem.* **1982**, *86*, 161.
(18) Johnson, B. P.; Khaledi, M. G.; Dorsey, J. G. *J. Chromatogr.* **1987**, *384*, 221.
(19) Johnson, B. P.; Khaledi, M. G.; Dorsey, J. G. *Anal. Chem.* **1986**, *58*, 2354.
(20) Åkesson, E.; Walker, G. C.; Barbara, P. F. *J. Chem. Phys.* **1991**, *95*, 4188.
(21) Åkesson, E.; Johnson, A. E.; Levinger, N. E.; Gilbert, G. C.; DuBruil, T. P.; Barbara, P. F. *J. Chem. Phys.* **1992**, *96*, 7859.
(22) Levinger, N. E.; Johnson, A. E.; Walker, G. C.; Barbara, P. F. *Chem. Phys. Lett.* **1992**, *196*, 159.
(23) Walker, G. C. Ph.D. Thesis, University of Minnesota, 1991.
(24) Walker, G. C.; Åkesson, E.; Johnson, A. E.; Levinger, N. E.; Barbara, P. F. *J. Phys. Chem.* **1992**, *96*, 3728.
(25) Johnson, A. E.; Levinger, N. E.; Jarzeba, W.; Schlief, R. E.; Kliner, D. A. V.; Barbara, P. F. *Chem. Phys.* **1993**, *176*, 555.
(26) Barbara, P. F.; Walker, G. C.; Smith, T. P. *Science* **1992**, *256*, 975.
(27) Zhu, J.; Rasaiah, J. C. *J. Chem. Phys.* **1994**, *101*, 9966.
(28) Gayathri, N.; Bagchi, B. *J. Chim. Phys.* **1996**, *93*, 1652.
(29) Maroncelli, M. *J. Mol. Liq.* **1993**, *57*, 1.
(30) Jimenez, R.; Fleming, G. R.; Kumar, P. V.; Maroncelli, M. *Nature* **1994**, *369*, 471.
(31) Rosenthal, S. J.; Xie, X.; Du, M.; Fleming, G. R. *J. Chem. Phys.* **1991**, *95*, 4715.
(32) Horng, M. L.; Gardecki, J. A.; Papazyan, A.; Maroncelli, M. *J. Phys. Chem.* **1995**, *99*, 17311.
(33) Gardecki, J.; Horng, M. L.; Papazyan, A.; Maroncelli, M. *J. Mol. Liq.* **1995**, *65*, 49.
(34) Maroncelli, M.; Fleming, G. R. *J. Chem. Phys.* **1988**, *89*, 5044.
(35) Maroncelli, M. *J. Chem. Phys.* **1991**, *94*, 2084.
(36) Carter, E. A.; Hynes, J. T. *J. Chem. Phys.* **1991**, *94*, 5961.
(37) Maroncelli, M.; Kumar, V. P.; Papazyan, A. *J. Phys. Chem.* **1993**, *97*, 13.
(38) Ladanyi, B. M.; Stratt, R. M. *J. Phys. Chem.* **1996**, *100*, 1266.
(39) Ladanyi, B. M.; Stratt, R. M. *J. Phys. Chem.* **1995**, *99*, 2502.
(40) Stratt, R. M.; Cho, M. *J. Chem. Phys.* **1994**, *100*, 6700.
(41) Bixon, M.; Jortner, J. *Chem. Phys.* **1993**, *176*, 467.
(42) Zong, Y.; McHale, J. L. *J. Chem. Phys.* **1997**, *106*, 4963.
(43) Lobaugh, J.; Rossky, P. J. *J. Phys. Chem.*, submitted.
(44) Warshel, A.; Karplus, M. *J. Am. Chem. Soc.* **1972**, *94*, 5612.
(45) Warshel, A.; Lappicirella, A. *J. Am. Chem. Soc.* **1981**, *103*, 4664. Warshel, A.; *Nature* **1976**, *260*, 679. Warshel, A.; Chu, Z. T.; Hwang, J.-K. *Chem. Phys.* **1991**, *158*, 303.
(46) Tully, J. C. *J. Chem. Phys.* **1990**, *93*, 1061.
(47) Pariser, R.; Parr, R. G. *J. Chem. Phys.* **1953**, *21*, 466.
(48) Pariser, R.; Parr, R. G. *J. Chem. Phys.* **1953**, *21*, 767.
(49) Pople, J. A. *Trans. Faraday Soc.* **1953**, *49*, 1375.
(50) Edwards, D. M. F.; Madden, P. A.; McDonald, I. R. *Mol. Phys.* **1984**, *51*, 1141.
(51) Bailey, M. L. *Theor. Chim. Acta (Berlin)* **1969**, *13*, 56.
(52) Nishimoto, K.; Forster, L. S. *Theor. Chim. Acta* **1966**, *4*, 155.
(53) Yamaguchi, Y.; Osamura, Y.; Goddard, J. D.; Schaefer, H. F., III *A New Dimension to Quantum Chemistry: Analytic Derivative Methods in Ab Initio Molecular Electronic Structure Theory*; Oxford University Press: Oxford, 1994; p 471.
(54) Pulay, P. In *Ab initio Methods in Quantum Chemistry-II*; Lawley, K. P., Ed.; John Wiley & Sons Ltd.: New York, 1987; Vol. 69.
(55) Pople, J. A.; Krishnan, R.; Schlegel, H. B.; Binkley, J. S. *Int. J. Quantum Chem.: Quantum Chem. Symp.* **1979**, *13*, 225.
(56) Handy, N. C.; Schaefer, H. F., III *J. Chem. Phys.* **1984**, *81*, 5031.
(57) Hurley, M. M.; Hammes-Schiffer, S. *J. Phys. Chem.*, in press.
(58) Tully, J. C. In *Dynamics of Molecular Collisions, Part B*; Miller, W. H., Ed.; Plenum Press: New York, 1976; Vol. 2, p 217.
(59) Stewart, J. J. P.; Seiler, F. J. Quantum Chemistry Program Exchange, Indiana University, 1990.
(60) Hwang, J.-K.; Warshel, A. *J. Am. Chem. Soc.* **1987**, *109*, 715. Warshel, A. Calculations of Vibronic Transitions of Conjugated Molecules (unpublished).
(61) Eckart, C. *Phys. Rev.* **1935**, *47*, 552.
(62) Wilson, E. B.; Decius, J. C.; Cross, P. C. *Molecular Vibrations the Theory of Infrared and Raman Vibrational Spectra*; Dover Publications, Inc.: New York, 1980.
(63) Hammes-Schiffer, S.; Tully, J. C. *J. Chem. Phys.* **1994**, 4657.
(64) Murell, J. N.; Harget, A. J. *Semiempirical Self-Consistent Molecular-Orbital Theory of Molecules*; Wiley-Interscience: London, 1972.
(65) Pickett, H. M.; Strauss, H. L. *J. Am. Chem. Soc.* **1970**, *92*, 7281.
(66) Ciccotti, G.; Ferrario, M.; Ryckaert, J.-P. *Mol. Phys.* **1982**, *47*, 1253.
(67) Linderberg, J. *Chem. Phys. Lett.* **1967**, *1*, 39.
(68) Atkins, P. W. *Molecular Quantum Mechanics*; Oxford University Press: Oxford, 1983.